Revealing layers of pristine oriented crystals embedded within deep ice clouds using differential reflectivity and the co-polar correlation coefficient

AGU PUBLICATIONS

JGR

Journal of Geophysical Research: Atmospheres

RESEARCH ARTICLE
10.1002/2017JD026754

Key Points:
- A novel polarimetric radar technique to reveal pristine oriented ice crystals embedded in deep ice cloud is presented
- Measurements of the copolar correlation coefficient can remove ambiguity in differential reflectivity measurements of ice particle mixtures

Correspondence to:
W. J. Keat,
william.keat@reading.ac.uk

Citation:
Keat, W. J., & Westbrook, C. D. (2017). Revealing layers of pristine oriented crystals embedded within deep ice clouds using differential reflectivity and the copolar correlation coefficient. *Journal of Geophysical Research: Atmospheres, 122*. https://doi.org/10.1002/2017JD026754

Received 3 APR 2017
Accepted 20 SEP 2017
Accepted article online 25 SEP 2017

Revealing Layers of Pristine Oriented Crystals Embedded Within Deep Ice Clouds Using Differential Reflectivity and the Copolar Correlation Coefficient

W. J. Keat[1] **and C. D. Westbrook**[1]

[1] Department of Meteorology, University of Reading, Earley Gate, Reading, UK

Abstract Pristine ice crystals typically have high aspect ratios (≫ 1), have a high density and tend to fall preferentially with their major axis aligned horizontally. Consequently, they can, in certain circumstances, be readily identified by measurements of differential reflectivity (Z_{DR}), which is related to their average aspect ratio. However, because Z_{DR} is reflectivity weighted, its interpretation becomes ambiguous in the presence of even a few, larger aggregates or irregular polycrystals. An example of this is in mixed-phase regions that are embedded within deeper ice cloud. Currently, our understanding of the microphysical processes within these regions is hindered by a lack of good observations. In this paper, a novel technique is presented that removes this ambiguity using measurements from the 3 GHz Chilbolton Advanced Meteorological Radar in Southern England. By combining measurements of Z_{DR} and the copolar correlation coefficient (ρ_{hv}), we show that it is possible to retrieve both the relative contribution to the radar signal and "intrinsic" Z_{DR} (Z^{P}_{DRI}) of the pristine oriented crystals, even in circumstances where their signal is being masked by the presence of aggregates. Results from two case studies indicate that enhancements in Z_{DR} embedded within deep ice clouds are typically produced by pristine oriented crystals with Z^{P}_{DRI} values between 3 and 7 dB (equivalent to 5–9 dB at horizontal incidence) but with varying contributions to the radar reflectivity. Vertically pointing 35 GHz cloud radar Doppler spectra and in situ particle images from the Facility for Airborne Atmospheric Measurements BAe-146 aircraft support the conceptual model used and are consistent with the retrieval interpretation.

1. Introduction

Microphysical processes occurring within mixed-phase clouds dictate the clouds' radiative properties (Comstock et al., 2007; Solomon et al., 2007), evolution, and lifetime (Morrison et al., 2012) and are fundamental to the production of precipitation (Mülmenstädt et al., 2015). The effective modeling of these processes depends on accurate representations of the ice crystal scattering properties, fall speeds, and primary and secondary ice nucleation mechanisms, which are uncertain (Harrington et al., 1999; Jiang et al., 2000; Morrison et al., 2003). Complex interactions and feedbacks between incoming and outgoing radiation, cloud dynamics, and microphysics make them particularly challenging to understand. Consequently, models struggle to correctly simulate the properties and processes occurring in mixed-phase clouds (Bodas-Salcedo et al., 2008; Klein et al., 2009; Morrison et al., 2009), and they are one of the greatest sources of uncertainty in future climate projections (Gregory & Morris, 1996; Mitchell et al., 1989; Senior & Mitchell, 1993; Sun & Shine, 1994). A key reason for this lack of understanding is a deficiency of good observations and techniques to observe mixed-phase clouds.

In mixed-phase conditions, pristine crystals are known to grow rapidly via the Bergeron-Findeison process; their habit is a function of the environmental temperature and supersaturation in which they form and grow. Their shape determines their scattering properties, growth rate, and fall speeds, hence cloud scattering properties, microphysical evolution, precipitation rate, and cloud lifetime. Furthermore, estimates of ice water content or number concentration require accurate knowledge of ice particle shape (Westbrook & Heymsfield, 2011). These pristine crystals typically have a high density and tend to fall with their major axes aligned horizontally (Cho et al., 1981; Sassen, 1980; Westbrook et al., 2010). This property makes dual-polarization radar a powerful tool for investigating the microphysical properties and processes within mixed-phase clouds, as the

preferential alignment of these crystals produces a larger backscatter in the horizontal (*H*) than the vertical (*V*) polarization.

Several studies have noted the existence of strong polarimetric radar signatures embedded within deep ice clouds (Andrić et al., 2013; Bechini et al., 2013; Hall et al., 1984; Hogan et al., 2002, 2003; Kennedy & Rutledge, 2011; Schrom et al., 2015; Wolde & Vali, 2001). Kennedy and Rutledge (2011) observed significant increases in specific differential phase (K_{DP}) embedded in a deep ice cloud at temperatures of about −15°C. By modeling a mixture of aggregates and pristine oriented crystals as oblate spheroids and performing T-matrix scattering calculations, they conclude that this signature was caused by the presence of dendritic particles with diameters of 0.8–1.2 mm with bulk densities greater than 0.3 g cm^{-3}. Similar enhancements of K_{DP} from 27 days of stratiform precipitation using X- and C-band radar measurements were reported by Bechini et al. (2013). They show that for over 70% of cases the maximum value of K_{DP} above the freezing level was located between −10 and −18°C. Like Kennedy and Rutledge (2011), they conclude that the enhancement was most likely produced by dendritic crystals. Furthermore, Bechini et al. (2013) present evidence that these enhanced K_{DP} signatures aloft are positively correlated with surface precipitation rate in stratiform rainfall, suggesting that this embedded ice growth is important. In combination with generalized multiparticle Mie scattering calculations, Schrom et al. (2015) use X-band measurements of Z_H, Z_{DR}, and K_{DP} to retrieve particle size distributions of plate and dendritic crystals at around −15°C. However, their method relies heavily on a priori assumptions about the ice particle size distribution and crystal size-aspect ratio relationships. Using a two-moment bulk microphysical model coupled with electromagnetic scattering calculations, Andrić et al. (2013) attempted to reconcile vertical profiles of observed and modeled radar reflectivity (Z_H), differential reflectivity (Z_{DR}), copolar correlation coefficient (ρ_{hv}), and K_{DP} at S-band. The model microphysics scheme, which included ice crystal nucleation, depositional growth, and aggregation, was able to reproduce the shape of the observed profile features, which suggests that vapor deposition and aggregation are able to explain most of the observed radar signatures. However, the magnitudes of the predicted radar variables were not accurately reproduced, implying microphysical processes either are not correctly represented or are missing.

Using the dual polarized S-band (3 GHz) Chilbolton Advanced Meteorological Radar (CAMRa) situated in Southern England in conjunction with in situ Johnson-Williams liquid water content measurements from on board an aircraft, Hogan et al. (2002) showed that the presence of elevated Z_{DR} measurements (> 3 dB) embedded within deep ice clouds tended to be associated with supercooled liquid water (SLW) and, therefore, acts as a proxy for mixed-phase conditions. In this particular case, the elevated Z_{DR} signature was produced by columns which were speculated to have been produced by the Hallett-Mossop process (Hallett & Mossop, 1974). A later study comparing polarimetric radar measurements in deep ice cloud with colocated lidar measurements (which readily detects SLW droplets) from on board an aircraft confirmed elevated Z_{DR} occurred in regions of SLW (Hogan et al., 2003).

For crystals falling with a preferential alignment, Z_{DR} is predominantly a measure of their reflectivity-weighted mean aspect ratio (which is defined as the ratio of major to minor axes throughout this paper). Therefore, it is key for investigating the microphysics of mixed-phase clouds since crystal shape is related to the microphysical processes that formed them and the conditions in which they grow. Unfortunately, the interpretation of Z_{DR} measurements becomes ambiguous when more than one crystal habit is present. The radar signal often becomes dominated by the presence of irregularly shaped polycrystals, or relatively few large aggregates (Bader et al., 1987; Hogan et al., 2002), which have Z_{DR} close to 0 dB and typically contribute most to the total reflectivity (and hence the overall Z_{DR} of the mixture). This masks the contribution that pristine oriented crystals make to Z_{DR}. Korolev et al. (2000) show that in thick stratiform ice cloud, 84% of ice particles >125 μm are irregularly shaped polycrystals or aggregates (Stoelinga et al., 2007) and that pristine crystals were observed relatively infrequently and typically embedded within larger zones of these irregularly shaped crystals on scales of approximately 100 m. In order to fully utilize Z_{DR} measurements to identify pristine ice crystals in deep ice clouds, the masking effect of aggregates must be removed. The aim of this paper is to present a technique that uses the novel combination of Z_{DR} and ρ_{hv} to "unmask" the contribution of pristine oriented ice crystals to the observed radar reflectivity, allowing the information contained within Z_{DR} measurements to be useful even in aggregated regions.

2. Polarimetric Radar Variables

In this section, the dual-polarization radar variables that will be used extensively in this paper are described.

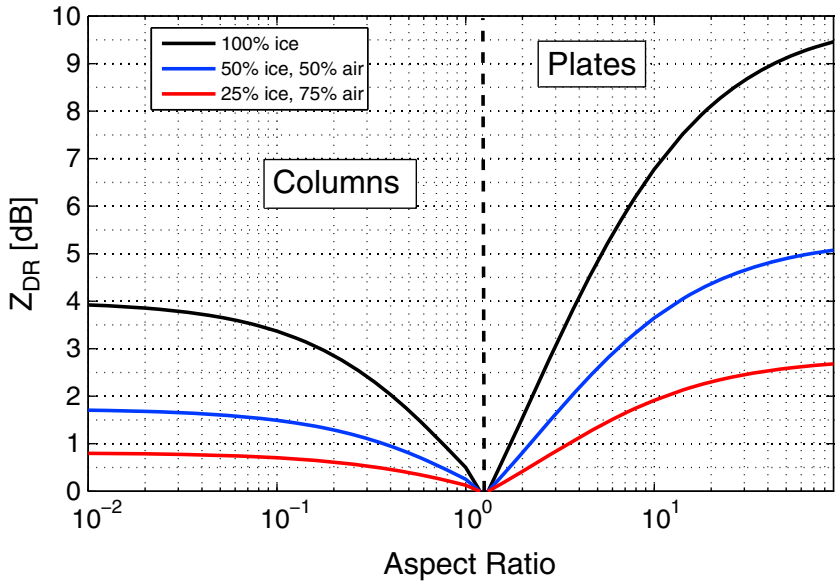

Figure 1. Differential reflectivity of pristine plates and columns as function of their aspect ratio when viewed at horizontal incidence with their major axes aligned horizontally.

2.1. Differential Reflectivity (Z_{DR})

Differential reflectivity is defined as the ratio of radar reflectivities in the horizontal H and V polarizations:

$$Z_{DR} = 10 \log_{10} \left(\frac{Z_h}{Z_v} \right) \quad \text{(dB)} \tag{1}$$

where Z_h and Z_v are the radar reflectivities in the H and V polarizations, respectively (in units of mm^6 m^{-3}). It is therefore a measure of the shape, density, and alignment of hydrometeors (Seliga & Bringi, 1976). Positive values occur when the backscatter in the H polarization is larger than in the V polarization. This is the case for oblate rain drops or ice crystals aligned with their major axis horizontally aligned. In rainfall, this property can be exploited to improve estimates of rain rate due to the unique relationship between drop size and shape (Seliga & Bringi, 1976). Its interpretation in ice clouds is more ambiguous; the shapes and sizes of ice particles are generally not uniquely related. The Z_{DR} of pristine oriented crystals, however, can be readily predicted using Gans theory. Figure 1 shows the Z_{DR} of pristine ice crystals of various aspect ratios and air-ice mixtures computed using the modified Gans equations of Westbrook (2014). Due to their high-density, pristine crystals aligned with their major axes horizontal can produce very large Z_{DR} signatures. This is particularly true of high-density plates, which can theoretically produce a Z_{DR} measurement up to 10 dB (e.g., Hogan et al., 2002). In any case, the larger the volume fraction of air in these crystals, the lower their "effective" dielectric factor, which is proportional to the bulk density of the air-ice mixture (Batten, 1973). Aggregate crystals consist largely of air and have aspect ratios of only ≈ 0.63 Westbrook et al. (2004) and, therefore, produce a low Z_{DR} (typically 0–0.3 dB). Since these crystals have a large mass and Z_{DR} is reflectivity weighted (i.e., effectively mass^2 weighted), the result is that even a small number of these crystals can dominate the Z_{DR} signal from smaller pristine crystals (Bader et al., 1987).

2.2. The Copolar Correlation Coefficient (ρ_{hv})

The copolar correlation coefficient is defined as (Bringi & Chandrasekar, 2001):

$$\rho_{hv} = \frac{\sum S_{HH} S_{VV}^*}{\sqrt{\sum |S_{HH}|^2 \sum |S_{VV}|^2}}. \tag{2}$$

where $\sum S_{HH}$ and $\sum S_{VV}$ are the sums of the copolar elements of the backscattering matrix from each particle in the radar sample volume and the asterisk indicates the complex conjugate. It can be estimated by cross-correlating successive power or complex (in-phase, I, and quadrature, Q) measurements. Among other things, ρ_{hv} is a measure of shape diversity within a sample volume. This property makes it complimentary to

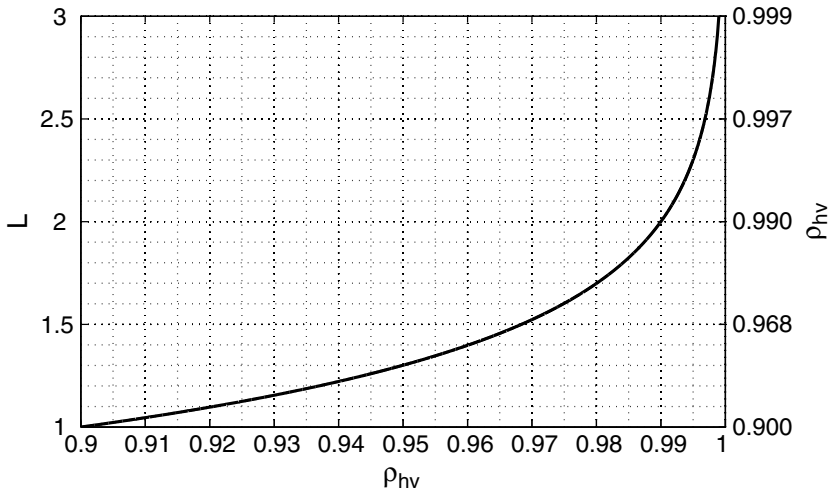

Figure 2. The relationship between $L = -\log_{10}(1 - \rho_{hv})$ and ρ_{hv}.

hydrometeor shape measurements of Z_{DR}. It has therefore been used to identify the melting layer (Brandes & Ikeda, 2004; Caylor & Illingworth, 1989; Giangrande et al., 2008; Tabary et al., 2006), ground clutter (e.g., Tang et al., 2014), and rain-hail mixtures (Balakrishnan & Zrnic, 1990); ρ_{hv} also been used to aid interpretation of polarimetric signatures of ice (e.g., Andrić et al., 2013; Moisseev et al., 2015) and in retrieving the shape of drop-size distributions (Keat et al., 2016). In embedded mixed-phase clouds (containing a mixture of newly formed pristine oriented crystals and aggregates or irregular polycrystals falling from above), one would expect reductions of ρ_{hv} to be colocated with enhanced Z_{DR}. Such reductions have been noted (Andrić et al., 2013; Moisseev et al., 2015), but the quantitative microphysical information that is contained within ρ_{hv} is yet to be fully exploited. In order to enable the quantitative use of ρ_{hv}, one must be able to quantify the uncertainty on its measurement. Keat et al. (2016) introduce a new variable: $L = -\log_{10}(1 - \rho_{hv})$ which allows rigorous confidence intervals on each ρ_{hv} sample to be derived, using

$$\sigma_L = \frac{2}{\ln 10} \times \frac{1}{\sqrt{N_{IQ} - 3}} \tag{3}$$

for $N_{IQ} \gg 3$, where N_{IQ} is the number of independent I and Q samples used to estimate ρ_{hv}. N_{IQ} can readily be estimated using only the observed Doppler spectral width (σ_v):

$$N_{IQ} = \frac{T_{\text{dwell}}}{\tau_{IQ}} = \frac{2\sqrt{2\pi}\sigma_v T_{\text{dwell}}}{\lambda} \tag{4}$$

where T_{dwell} is the dwell time, τ_{IQ} is the time to independence for I and Q samples (Doviak & Zrnic, 2006), and λ is the radar wavelength.

Furthermore, the Gaussian nature of distributions of L prevent the introduction of a bias during averaging many ρ_{hv} samples (Keat et al., 2016). These statistical advantages mean that the use of L is preferred over ρ_{hv} and is chosen for use throughout this paper. The relationship between L and ρ_{hv} is shown in Figure 2.

3. Retrieval Development

In this section, a technique to separate the reflectivity of pristine oriented crystals from coexisting irregular polycrystals or aggregates using polarimetric radar is described. Hereafter, the terms aggregates and polycrys-

Table 1
Theoretical Observations of ρ_{hv} and Z_{DR} for Regions of (I) Aggregates Only, (II) Pristine Oriented Crystals Only, and (III) a Mixture of Pristine Oriented Crystals and Aggregates

	Expected ρ_{hv}	Expected Z_{DR}
Aggregates only	≈ 1	Z^A_{DRI} (0–0.3 dB)
Pristine crystals only	≈ 1	Z^P_{DRI}
Pristine crystals and aggregates	< 1	$Z^A_{DRI} < Z_{DR} < Z^P_{DRI}$

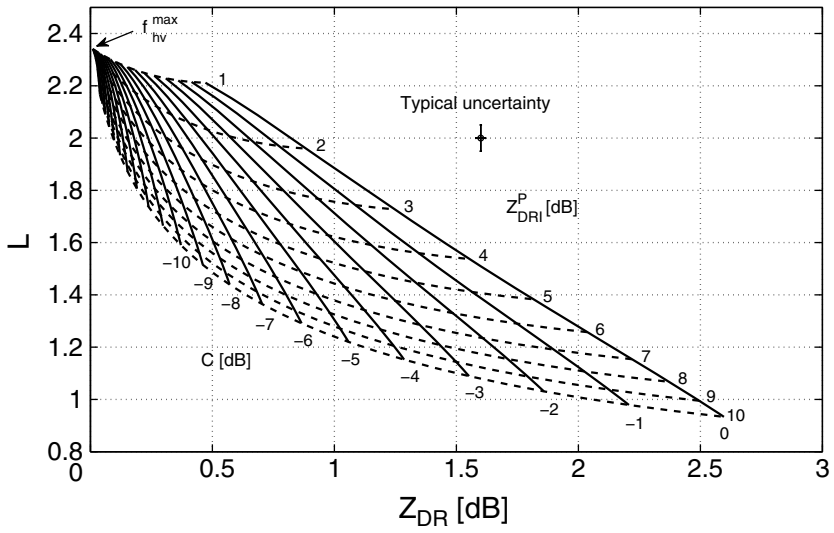

Figure 3. Schematic illustrating predicted C (solid isopleths) and Z^P_{DRI} (dashed isopleths) as a function of observed L and Z_{DR} based on equations (9) and (13). Isopleths of C ranging from −10 to 0 dB and Z^P_{DRI} ranging from 1 to 10 dB are labeled. A representative $f^{\max}_{hv}$ (see section 3.2) and typical measurement uncertainties are shown (σ_L=0.05 and $\sigma_{Z_{\mathrm{DR}}}$ = 0.02 dB; see text for details).

tals will be used interchangeably to refer to the pseudospherical "background" ice particles that mask the signal from pristine crystals. Fundamentally, the retrieval combines information about the reflectivity-weighted particle aspect ratio (provided by Z_{DR} measurements) with information regarding the diversity of shapes within a radar sample volume (provided by ρ_{hv}). Qualitatively, if only aggregates are present in a radar sample volume, Z_{DR} will be low (typically 0–0.3 dB), and since all particle shapes are the same ρ_{hv} will be high (close to 1). If only pristine oriented crystals are present, the measured Z_{DR} will be equal to the "intrinsic" Z_{DR} (Z^P_{DRI}) of the pristine oriented crystals, as they are the only crystal habit. For the same reason, ρ_{hv} will again be close to 1. Now, consider the situation where pristine oriented crystals are growing among aggregates. The observed Z_{DR} will be related to the reflectivity-weighted aspect ratio of all the particles in the sample volume, and, since there is now more than one particle shape, ρ_{hv} will be <1. These situations are summarized in Table 1. With some simple assumptions, we will show that each pair of measured ρ_{hv} and Z_{DR} can be uniquely related to the relative contribution pristine oriented crystals make to the observed radar reflectivity compared to aggregates (C) and their Z^P_{DRI}.

The following assumptions are made: (i) Embedded mixed-phase regions consist only of pristine crystals and pseudospherical aggregates that can be represented by two distinct ice crystal populations. (ii) The "intrinsic" Z_{DRI} of the aggregates is fixed and assumed to be 0 dB. (iii) Pristine oriented crystals have a fixed aspect ratio and fall with their major axis aligned horizontally (with a fixed canting angle of 0°). The sensitivity to assumptions (ii) and (iii) are discussed in sections 5 and 6, respectively.

3.1. Derivation

Under assumption (i), linear Z_{DR} (Z_{dr}) can be written in terms of the individual radar reflectivity contributions from each crystal type:

$$Z_{\mathrm{dr}} = \frac{\sum |S_{HH}|^2}{\sum |S_{VV}|^2} = \frac{Z_h}{Z_v} = \frac{Z^A_h + Z^P_h}{Z^A_v + Z^P_v} \tag{5}$$

where $\sum S_{HH}$ and $\sum S_{VV}$ are the sums of the copolar elements of the backscattering matrix over all ice crystals and the superscripts A and P correspond to the aggregate and pristine crystal contributions, respectively. For convenience, we will normalize S_{HH} and S_{VV} such that $\sum |S_{HH}|^2 = Z_h$ and $\sum |S_{VV}|^2 = Z_v$. Dividing both the numerator and denominator by Z_h, and invoking assumption (ii), $Z^A_h = Z^A_v$:

$$Z_{\mathrm{dr}} = \frac{1 + \frac{Z^P_h}{Z^A_h}}{\frac{Z^A_v}{Z^A_h} + \frac{Z^P_v}{Z^A_h}}. \tag{6}$$

Under assumption (iii), the "intrinsic" Z_{dr} of the pristine crystals (the Z_{dr} that would be observed if only the pristine crystals were sampled by the radar) can be defined as

$$Z^P_{\text{dri}} = \frac{\sum^P |S_{HH}|^2}{\sum^P |S_{VV}|^2} = \frac{Z^P_h}{Z^P_v}. \tag{7}$$

By defining the relative contribution of Z_h from the pristine oriented crystals to Z_h of the aggregates as

$$c = \frac{\sum^P |S_{HH}|^2}{\sum^A |S_{HH}|^2} = \frac{Z^P_h}{Z^A_h}, \tag{8}$$

the observed Z_{dr} of the mixture can be written as

$$Z_{\text{dr}} = \frac{1+c}{1+\frac{c}{Z^P_{\text{dri}}}}. \tag{9}$$

Similarly, for ρ_{hv}, beginning with its definition (equation (2)) and splitting into the contributions from each crystal type:

$$\rho_{hv} = \frac{\sum^A S_{HH}S^*_{VV} + \sum^P S_{HH}S^*_{VV}}{\sqrt{\left(\sum^A |S_{HH}|^2 + \sum^P |S_{HH}|^2\right)\left(\sum^A |S_{VV}|^2 + \sum^P |S_{VV}|^2\right)}}. \tag{10}$$

Recognizing that

$$|S^P_{VV}|^2 = \frac{|S^P_{HH}|^2}{Z_{\text{dri}}}{}^P, \tag{11}$$

if aggregates are spherical (assumption ii) and all pristine crystals have a fixed aspect ratio (assumption iii), then

$$\rho_{hv} = \frac{\sum^A |S_{HH}|^2 + \sum^P |S_{HH}|^2/\sqrt{Z^P_{\text{dri}}}}{\sqrt{\left(Z^A_h + Z^P_h\right)\left(Z^A_v + Z^P_v\right)}}. \tag{12}$$

Finally, dividing both the numerator and denominator by Z^A_h yields the observed copolar correlation coefficient for the mixture:

$$\rho_{hv} = \frac{1+\frac{c}{\sqrt{Z^P_{\text{dri}}}}}{\sqrt{(1+c)\times\left(1+\frac{c}{Z^P_{\text{dri}}}\right)}} \tag{13}$$

The imaginary components of S_{HH} and S_{VV} are ignored in this derivation; absorption is very small at these wavelengths for ice ($\text{Im}(S_{HH}) \ll \text{Re}(S_{HH})$). The two measurements, ρ_{hv} and Z_{DR}, can now be directly related to the two "unknown" parameters, c and Z^P_{dri}. In what follows and during the retrieval, these parameters are expressed in logarithmic units ($C = \log_{10}(c)$ and $Z^P_{\text{DRI}} = 10\log_{10}(Z^P_{\text{dri}})$).

Given the preferential statistical characteristics of the variable L over ρ_{hv} (Keat et al., 2016), equations (9) and (13) are used to create look-up tables for L and Z_{DR} for C ranging between −20 and 0 dB, and Z^P_{DRI} between 0.1 and 10 dB. Figure 3 shows how measurements of L and Z_{DR} are theoretically related to C and Z^P_{DRI}. For the retrieval, the uncertainty on each L (σ_L) and Z_{DR} ($\sigma_{Z_{\text{DR}}}$) measurement is calculated using equation (3) and the method of Bringi and Chandrasekar (2001), respectively. The "typical" uncertainty shown in this figure is the median σ_L and $\sigma_{Z_{\text{DR}}}$ for the data above the melting layer in Figure 4. From this figure, we can see that when the polarimetric signature is weak (high L, low Z_{DR}), the isopleths of C and Z^P_{DRI} are densely packed. The range of values that are encompassed by the illustrated typical measurement uncertainty is very large, resulting in large uncertainty in the retrieval. By the same argument, when the polarimetric signature is stronger (low L, high Z_{DR}), the divergence in the C and Z^P_{DRI} isopleths means that one is able to retrieve C and Z^P_{DRI} with much more certainty. The retrieved C and Z^P_{DRI} are obtained by minimizing the differences between the measured and predicted L and Z_{DR} values in the look-up table, weighted by their individual measurement uncertainty.

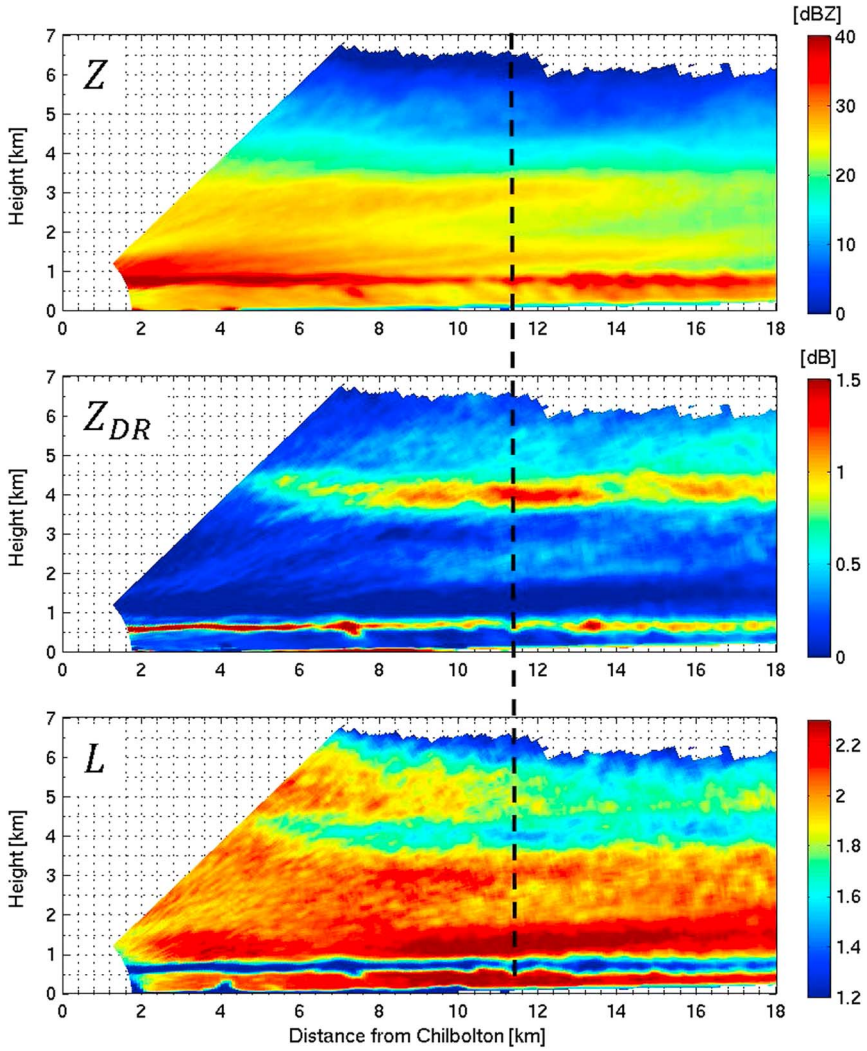

Figure 4. RHI scan at 1501 UTC on 31 January 2014 showing Z, Z_{DR}, and L. Data have been averaged to 1° and 300 m in range and is only shown for $SNR > 10$ dB. Note that L is the measured value and is significantly affected by low SNR above 4.5 km.

3.2. Practical Considerations

When making comparisons between theory and measurements, it is important to account for instrument error and uncertainties as well as other effects that could be misconstrued as being microphysical. Even for a completely monodisperse particle size distribution and infinite signal-to-noise ratio (SNR), effects such as an imperfect antenna will mean that measurements of ρ_{hv} will always be < 1. Following Keat et al. (2016), the maximum value that can be measured is referred to as the "inherent limit" of the antenna, $f_{hv}^{\max}$, and can be estimated as the "true" ρ_{hv} value when $Z_{DR} < 0.1$ dB. A representative $f_{hv}^{\max}$ of 0.995 ($L = 2.35$) is used to produce Figure 3. Predicted L is computed by multiplying ρ_{hv} in equation (13) by $f_{hv}^{\max}$.

In order to avoid biases in the retrieval due to poor SNR, look-up tables were created for a range of possible SNR values. The expected ρ_{hv} observation for each C and Z_{DRI}^{P} was adjusted by the factor f, calculated using the following equation from Bringi et al. (1983):

$$f = \frac{1}{\left(1 + \frac{1}{\mathrm{SNR}_H}\right)^{\frac{1}{2}} \left(1 + \frac{1}{\mathrm{SNR}_V}\right)^{\frac{1}{2}}}. \tag{14}$$

These values were then transformed into L space. This allows the retrieval to be applied even when SNR is relatively low (often in lower Z regions of ice cloud). However, doing this has the effect of increasing the impact of measurement uncertainty on retrieved C and Z_{DRI}^{P} uncertainty, as the same uncertainty in L and Z_{DR} now incorporates a larger range of C and Z_{DRI}^{P} values in the adjusted look-up tables. This method of accounting for

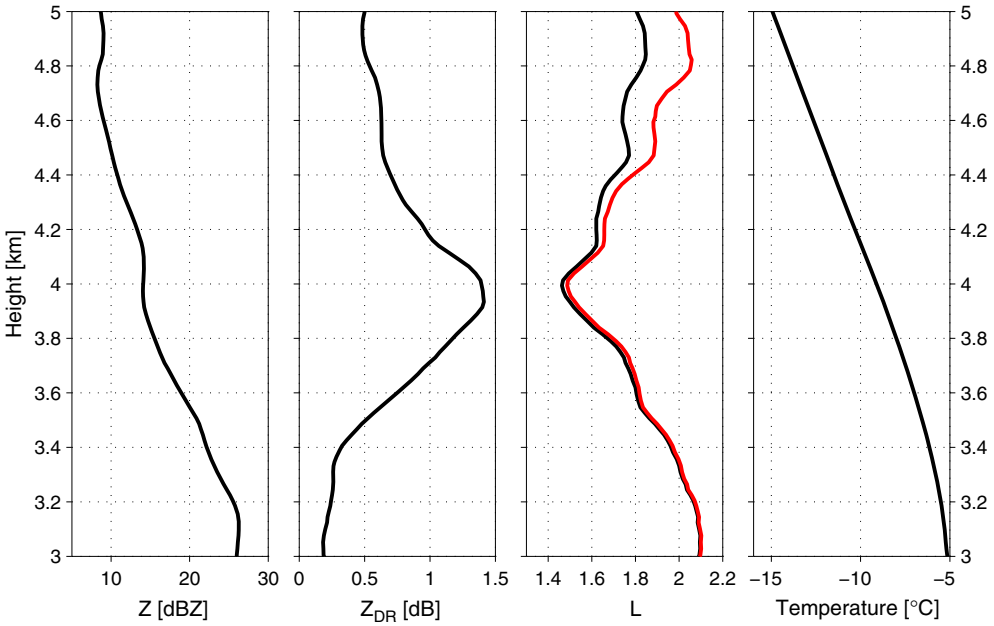

Figure 5. Vertical profiles of Z, Z_{DR}, L and temperature at 11.5 km from Chilbolton at 1501 UTC on 31 January 2014 (indicated by dashed black line in Figure 4). The red line is the "effective" L, that is, the L measurement adjusted for SNR to illustrate the "real" profile used in the retrieval.

SNR is preferable to correcting the observed ρ_{hv} value itself for SNR. Data where SNR is < 10 dB are not used in the retrieval. A more detailed discussion of the technical aspects of ρ_{hv} measurement can be found in Keat et al. (2016).

The retrieval technique also requires accurate calibration of Z_{DR}. This is done regularly for CAMRa (to within ± 0.1 dB) by making measurements of drizzle (low Z), which is known to have a Z_{DR} value of 0 dB.

4. Case Study I: 31 January 2014

This section demonstrates the retrieval technique applied measurements made on 31 January 2014. On this day, a warm front passed over the UK and was sampled by CAMRa. The radar boasts a very large antenna (25 m), making it the world's largest fully steerable meteorological radar. The resulting narrow one-way half power beamwidth (0.28°) makes it capable of very high resolution measurements. CAMRa is a coherent-on-receive magnetron system, transmitting alternate H and V polarized pulses with a pulse repetition frequency of 610 Hz (receiving in both H and V channels simultaneously). Therefore, to calculate ρ_{hv} (at zero lag), a cubic polynomial interpolation is used to estimate the H power at the V pulse timing and the V power at the H pulse timing and successive H and V powers are then correlated. Further details can be found in Keat et al. (2016). The full capabilities of this radar are discussed in Goddard et al. (1994).

Figure 4 shows the observed Z, Z_{DR}, and L for a range-height indicator (RHI) scan made at 1501 UTC. Data have been averaged over 10 rays (1°) and 4 range gates (300 m) to increase the number of independent I and Q samples and improve the precision of the measurements. The melting layer can be clearly identified as the thin layer of enhanced Z (>35 dBZ) at a height of ≈ 1 km. Colocated is an elevated Z_{DR} signature, which occurs as ice crystals with positive aspect ratios begin to melt and become water coated, increasing their dielectric factor and therefore radar reflectivity in each polarization. A decrease in L is also seen due to the mixture of shapes and phases in the melting layer. The polarimetric signature of interest can be identified at approximately 4 km in height.

Figure 5 shows a vertical profile of Z, Z_{DR}, L and temperature from the European Centre for Medium-Range Weather Forecasts operational weather forecast model. The location of this profile is indicated by the dashed black line in Figure 4. The black line in the L profile shows the measured values of L (influenced by SNR). The red line is L corrected for the effects of SNR using f from section 3.2. This is plotted in order to give a sense of the "effective" L that is used in the retrieval once the look-up tables have been adjusted for SNR (as discussed in section 3.2). The profile is only shown between the heights of 3 and 5 km, through the depth of the

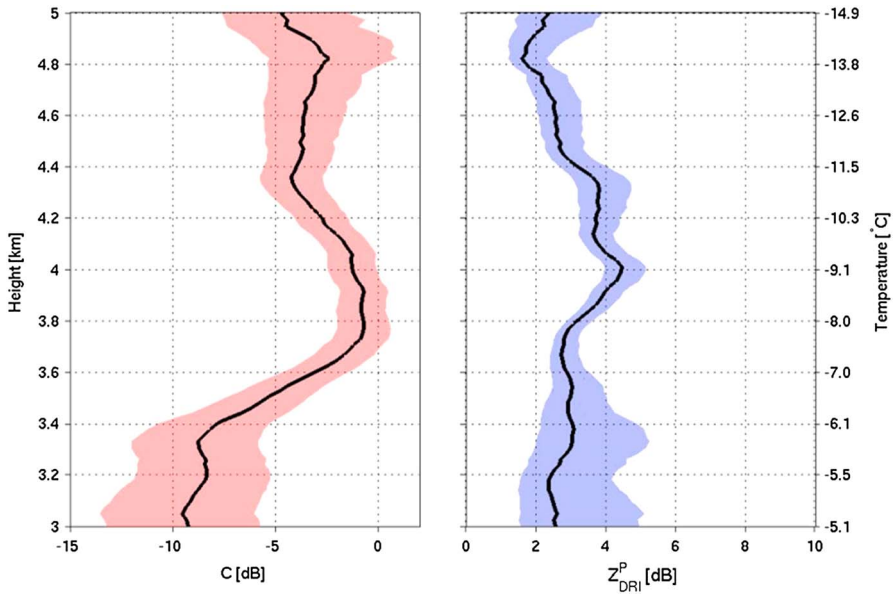

Figure 6. Vertical profile of retrieved C and Z^P_{DRI} as a function of height and temperature 11.5 km from Chilbolton at 1501 UTC on 31 January 2014. Z^A_{DRI} is assumed to be 0 dB.

polarimetric signature of interest. At a height of 5 km, Z is 10 dBZ, while Z_{DR} is around 0.5 dB. This is indicative of irregularly shaped polycrystals or pseudospherical aggregates. The SNR-adjusted L is 2 ($\rho_{hv} = 0.99$), indicating that the ice crystals producing this Z_{DR} have approximately the same shape. Descending below 4.8 km, Z and Z_{DR} begin to increase and L decreases with decreasing height. These trends continue until at 4 km, Z_{DR} reaches almost 1.5 dB and L reaches a minimum just below 1.5 ($\rho_{hv} = 0.97$). Interestingly, the L minimum occurs about 50 m higher and is shallower than the Z_{DR} maximum. This feature also appears in vertical profiles presented by Andrić et al. (2013).

Our microphysical interpretation of this profile is as follows. Pristine oriented crystals are nucleating at ≈ 4.8 km, presumably in a layer of SLW drops, some of which are nucleated to form new ice particles. The temperature at 4.8 km is ≈ −14°C, meaning these crystals are most likely to be plate like (Bailey & Hallett, 2009). These plates have positive aspect ratios and fall with their major axis aligned in the horizontal plane. This causes an increase in the reflectivity-weighted aspect ratio (increasing Z_{DR}) and an increase in the diversity of shapes in the sample volume (decreasing L), as they are forming among pseudospherical aggregate crystals. As these crystals continue to grow by vapor deposition, their contribution to Z increases, Z_{DR} increases, and L decreases, as the reflectivity of the pristine oriented crystals becomes comparable to that of the aggregates (C increases). The peaks in L and Z_{DR} at ≈ 4 km indicate the height at which the process of aggregation begins dominating over the vapor growth of pristine crystals. Between 4 and 3.4 km Z increases by 10 dB, corresponding with a rapid decrease in Z_{DR} to 0.3 dB and increase in L to 2. This is characteristic of aggregation; the particles in the volume are becoming larger and look more spherical to the radar, while overall shape diversity is decreasing. Just before the melting layer is reached, Z_{DR} is very low (≈ 0.2 dB), and L is very high (≈ 2.3), which is indicative of an aggregate-only crystal population.

Figure 6 shows retrieval profiles of C (left) and Z^P_{DRI} (right) for the observations shown in Figure 5. The shaded areas depict the uncertainty in the retrieval that results from measurement uncertainty in L and Z_{DR}. This range was calculated as the maximum and minimum possible retrieval values that could result from $L \pm \sigma_L$ and $Z_{DR} \pm \sigma_{Z_{DR}}$.

First, examining the profile between 5 and 4.4 km in height, the retrieval reveals that the observed Z_{DR} of ≈0.5 dB is in fact produced by pristine crystals with an intrinsic Z_{DR} of ≈ 2.5 dB. However, this signal is being masked; the relative contribution of the pristine oriented crystals to the radar reflectivity, C, is ≈ −3–4 dB (≈ 40% that of the aggregates). Fluctuations in Z^P_{DRI} appear to correspond to a fluctuations in measured L; indeed, inspection of Figure 3 reveals that the retrieved Z^P_{DRI} value is most influenced by changes along the L axis. Similarly, the relatively steady behavior of C can be explained by the fact that C is most influenced by changes in the Z_{DR} axis and Z_{DR} is more smoothly varying. Between 4.4 and 4 km, both C and Z^P_{DRI} increase. Plate crystals initially have aspect ratios close to 1:1, which increase as they grow to form thinner structures

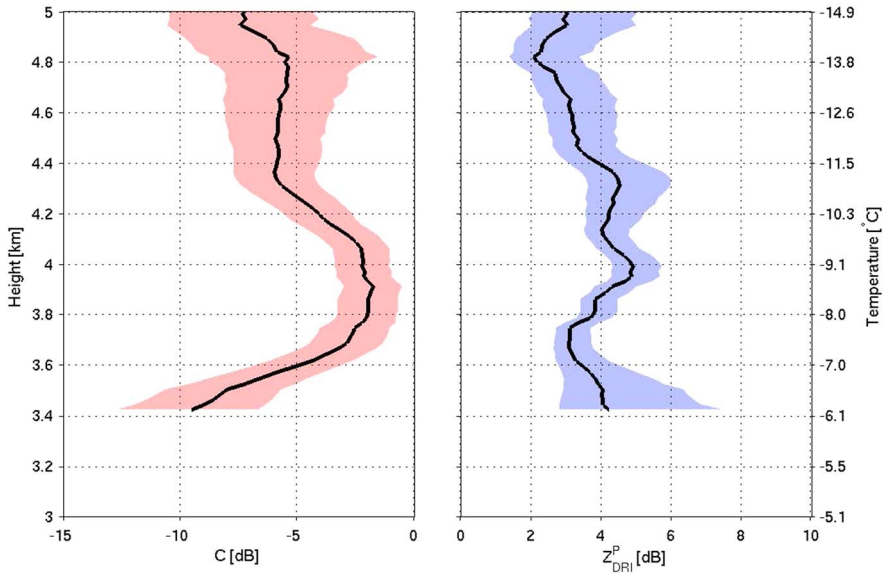

Figure 7. Vertical profile of retrieved C and Z^P_{DRI} as a function of height and temperature 11.5 km from Chilbolton at 1501 UTC on 31 January 2014. The retrieval is only shown when $C > -10$ dB. Z^A_{DRI} is assumed to be 0.15 dB.

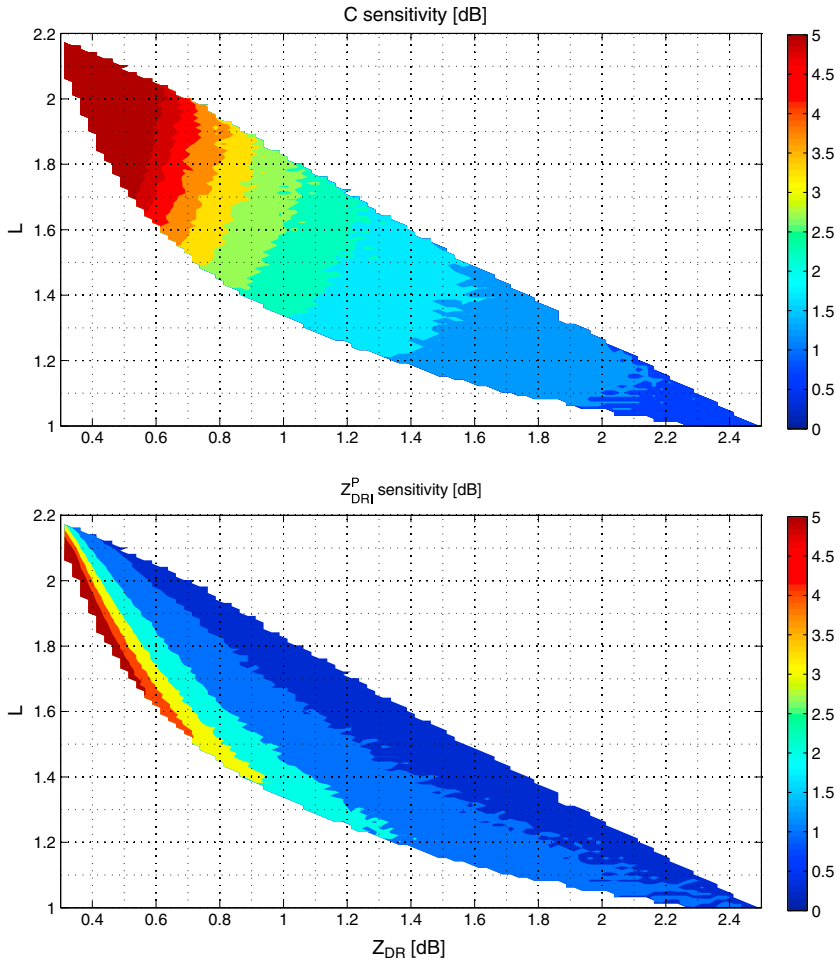

Figure 8. The sensitivity of retrieved C and Z^P_{DRI} to the assumption of Z^A_{DRI}, expressed as the difference between assuming Z^A_{DRI} = 0.3 dB as opposed to 0 dB.

(Takahashi et al., 1991). This is consistent with the increase in Z^P_{DRI} from ≈ 2 dB at 4.8 km to over 4 dB at 4 km in height. There is then a broad maximum in C between 4 and 3.7 km that corresponds to the location of the strongest Z_{DR} signature. Here the pristine crystals contribute their highest to the reflectivity; C is ≈ −1 dB (or 80% that of aggregates). This maximum C value is maintained down to about 3.7 km, while Z^P_{DRI} decreases back to 3 dB, where it remains approximately constant even as C decreases to −8 dB at 3.4 km. The reduction in C implies that the newly formed crystals are aggregating. This figure demonstrates how the retrieval is able to provide an interpretation of pristine ice crystal properties in deep frontal clouds that was previously unavailable.

5. Accounting for Nonspherical Aggregates

So far, the retrieval is based on the assumption that aggregates are perfect dielectric spheres to the radar. In nature, this is not necessarily the case; it has been argued in the literature that the mean Z_{DR} of dry and wet aggregates is typically nonzero but rarely exceeds 0.3 dB (Ryzhkov et al., 2005; Ryzhkov & Zrnic, 1998a). The Z_{DR} of the aggregates just above the melting layer in Figure 4 is ≈ 0.2 dB. Assuming aggregates are perfectly spherical rather than slightly nonspherical will result in some of the Z_{DR} signal being misattributed to the pristine oriented crystals. It will also cause Z^P_{DRI} to be overestimated; nonspherical aggregates are more similar in shape to pristine oriented crystals.

To account for these nonspherical aggregates, assumption (ii) is relaxed, and a fixed "intrinsic" Z_{dr} of aggregates is assumed, defined as

$$Z^A_{\mathrm{dri}} = \frac{Z^A_h}{Z^A_v}. \tag{15}$$

To include Z^A_{dri} as a variable in the retrieval, equation (9) can be slightly modified to

$$Z_{\mathrm{dr}} = \frac{1+c}{\frac{c}{Z^P_{\mathrm{dri}}} + \frac{1}{Z^A_{\mathrm{dri}}}}. \tag{16}$$

Similarly, equation (13) can be written as

$$\rho_{hv} = \frac{\frac{1}{\sqrt{Z^A_{\mathrm{dri}}}} + \frac{c}{\sqrt{Z^P_{\mathrm{dri}}}}}{\sqrt{(1+c)\times\left(\frac{1}{Z^A_{\mathrm{dri}}} + \frac{c}{Z^P_{\mathrm{dri}}}\right)}}. \tag{17}$$

Figure 7 shows the same profiles as Figure 6 but with an assumed Z^A_{DRI} of 0.15 dB. Broadly, the profile characteristics remain similar to the case when Z^A_{DRI} = 0 dB. Retrieved quantities are only shown where the polarimetric signature is strong enough to produce $C > -10$ dB, and the retrieval is deemed reliable. The two local maxima in Z^P_{DRI} are observed at the same heights, and the broad maximum in C is still present between 4.4 and 3.5 km. However, the magnitudes of the retrieved quantities are different. C has typically decreased at all heights, whereas Z^P_{DRI} has typically increased. The peak in C is now ≈ −3 dB not −1 dB, and typically Z^P_{DRI} values are now 5 rather than 3–4 dB. The retrieval uncertainty is also slightly larger, because the adjustment for Z^A_{DRI} puts the observed L and Z_{DR} into the more sensitive part of the forward model. This causes the same measurement uncertainty to span over a larger range of possible C and Z^P_{DRI} values. The precise magnitudes of these changes depend on the sensitivity of the forward model for each particular pair of L and Z_{DR} observations.

To investigate the sensitivity of the retrieval to the assumption of Z^A_{DRI}, L and Z_{DR} were forward modeled using Z^A_{DRI} values of 0 and 0.3 dB, covering the expected Z_{DR} range for aggregates. The sensitivity of the forward model is defined as the absolute difference in retrieved C and Z^P_{DRI} due to Z^A_{DRI} changing between these limits, for a given pair of L and Z_{DR} observations. The uncertainty in L and Z_{DR} is set to 0.05 and 0.02 dB, respectively, which is typical for the data used in the retrievals. Figure 8 shows the sensitivity of C (top) and Z^P_{DRI} (bottom) to this difference. Both C and Z^P_{DRI} are increasingly sensitive for higher L and lower Z_{DR}. This is not surprising, as the C and Z^P_{DRI} isopleths are almost indistinguishable for weak polarimetric signatures (see Figure 3). It is clear that C is most sensitive to the choice of Z^A_{DRI}, exhibiting sensitivity $\gtrsim$ 2.5 dB up to Z_{DR} = 1 dB. This sensitivity decreases as Z_{DR} increases; for Z_{DR} = 1.5 dB (the upper range of the data presented here), the sensitivity is 1–2 dB. The retrieved Z^P_{DRI} is also sensitive to the choice of Z^A_{DRI}, especially for low L (i.e., where retrieved Z^P_{DRI} values are highest). Above Z_{DR} = 1 dB, the sensitivity is typically 1–2 dB.

Although the retrieval outputs are sensitive to this assumption for weak polarimetric signatures, fortunately, it is when polarimetric signatures are stronger that the pristine oriented crystals are likely to be contributing most significantly to snow growth processes and the information from the retrieval is most useful. Clearly, care should be taken when interpreting the retrieval results for weak polarimetric signatures.

6. Accounting for Pristine Oriented Crystal Aspect Ratio Variability

Another assumption made in the retrieval is that all of the pristine oriented crystals have a fixed aspect ratio. In reality, ice crystals are nucleated at different depths within a SLW layer and can grow at different rates, leading to an eventual distribution of aspect ratios for a given crystal habit. Not accounting for a variety of crystal aspect ratios will cause the retrieved Z^P_{DRI} for a given L measurement to be overestimated. This is because the measured L will include a contribution from pristine crystal shape diversity which would be misinterpreted as being the result of pristine crystals with more extreme aspect ratios. It would also cause C to be underestimated for a given Z_{DR} measurement.

The forward modeled Z_{DR} values will not be affected by an increase in shape variety, as in what follows uniform distributions are defined about the mean Z^P_{DRI} value, such that the average Z^P_{DRI} remains the same. Therefore, Z_{DR} can be predicted using an equation identical to 9, but where Z^P_{DRI} should be interpreted as the reflectivity-weighted average of the Z^P_{DRI} distribution. The predicted L observation will be affected, as it is sensitive to any additional variability in shape. To account for this, an equation can be derived similarly to equation (13) using the definitions of c and Z^P_{dri} given by equations (7) and (8).

Starting from equation (10) and dividing both the numerator and denominator by Z^A_h, assuming initially that aggregates are spherical ($S_{HH} = S_{VV}$):

$$\rho_{hv} = \frac{1 + \frac{\sum^P S_{HH} S_{VV}}{Z^A_h}}{\sqrt{\left(1 + \frac{Z^P_h}{Z^A_h}\right)\left(\frac{Z^P_h}{Z^A_h} + \frac{Z^P_h}{Z^A_h}\right)}}. \tag{18}$$

Noting that in the numerator,

$$\frac{\sum^P S_{HH} S_{VV}}{Z^A_h} = \frac{Z^P_h}{Z^P_h} \times \frac{\sum^P S_{HH} S_{VV}}{Z^A_h} = c \times \frac{\sum^P S_{HH} S_{VV}}{Z^P_h}, \tag{19}$$

$$\begin{aligned} c \times \frac{\sum^P S_{HH} S_{VV}}{Z^P_h} &= c \times \frac{\sum^P S_{HH} S_{VV}}{\sqrt{\sum^P |S_{HH}|^2 \sum^P |S_{VV}|^2}} \times \sqrt{\frac{\sum^P |S_{VV}|^2}{\sum^P |S_{HH}|^2}} \\ &= c \times \rho^P_{hv} \times \sqrt{\frac{1}{Z^P_{\mathrm{dri}}}}, \end{aligned} \tag{20}$$

then

$$\rho_{hv} = \frac{1 + c \times \rho^P_{hv} \times \sqrt{\frac{1}{Z^P_{\mathrm{dri}}}}}{\sqrt{\left(1 + \frac{Z^P_h}{Z^A_h}\right)\left(\frac{Z^P_h}{Z^A_h} + \frac{Z^P_h}{Z^A_h}\right)}} \tag{21}$$

where ρ^P_{hv} is the copolar correlation coefficient that would result from a mixture of pristine crystals in the absence of any aggregates, characterizing the shape diversity of the pristine crystal population. Therefore,

$$\rho_{hv} = \frac{1 + c \times \rho^P_{hv} \times \sqrt{\frac{1}{Z^P_{\mathrm{dri}}}}}{\sqrt{(1 + c) \times \left(1 + \frac{c}{Z^P_{\mathrm{dri}}}\right)}}. \tag{22}$$

Note that this equation can be readily modified to include the effect of an arbitrary intrinsic differential reflectivity Z^A_{dri}:

$$\rho_{hv} = \frac{\frac{1}{\sqrt{Z^A_{\mathrm{dri}}}} + c \times \rho^P_{hv} \times \sqrt{\frac{1}{Z^P_{\mathrm{dri}}}}}{\sqrt{(1 + c) \times \left(\frac{1}{Z^A_{\mathrm{dri}}} + \frac{c}{Z^P_{\mathrm{dri}}}\right)}}. \tag{23}$$

The sensitivity of the retrieval to the assumption of a fixed aspect ratio is tested using the same method as that used to test the sensitivity to the assumption of Z^A_{DRI}. L and Z_{DR} were again forward modeled, but for each Z^P_{DRI} value a uniform distribution of Z^P_{DRI} with a width of 1 dB was assumed. Figure 9 shows the sensitivity of C (top) and Z^P_{DRI} (bottom) to assuming a uniform 1 dB distribution width compared to a fixed aspect ratio.

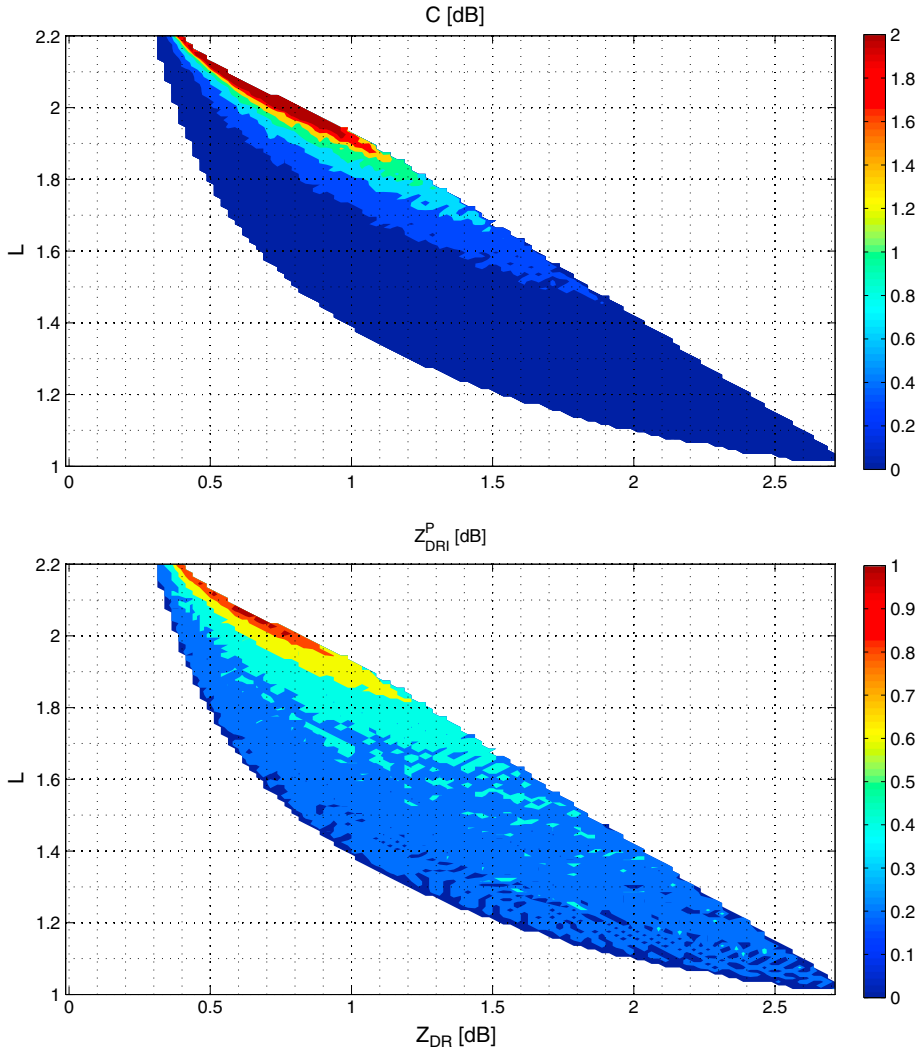

Figure 9. The sensitivity of retrieved C and Z^P_{DRI} to assuming a uniform Z^P_{DRI} distribution width of 1 dB compared to assuming a fixed aspect ratio.

Clearly, C and Z^P_{DRI} are much less sensitive to the assumption of a fixed aspect ratio than they are to the assumption of Z^A_{DRI}. The greatest sensitivity in both C and Z^P_{DRI} again occurs when the polarimetric signal is relatively weak ($L > 1.8$ and $Z_{DR} < 1$ dB). There is pronounced sensitivity to a distribution of pristine oriented crystal shapes for higher L (which corresponds to smaller predicted Z^P_{DRI} values). This is because the contribution to the reduction of L from pristine oriented crystal aspect ratio variability (ρ^P_{hv} in equation (21)) is larger when the Z^P_{DRI} distribution width is comparable in magnitude to the mean Z^P_{DRI} value. Again, the retrieved C is most sensitive to the assumption. For high L and low Z_{DR}, it is as large as 2 dB, but, for the majority of L and Z_{DR} values, the sensitivity is lower than 0.5 dB. Z^P_{DRI} is less sensitive overall and broadly less than 0.5 dB. The retrieval is therefore considered to be insensitive to pristine crystal shape variability except for when the polarimetric signature is very weak, which in any case is likely to be in circumstances where the pristine oriented crystals are not contributing significantly to snow growth processes.

7. Case Study II: 17 February 2016—Coincident Radar and In Situ Observations

On 17 February 2016, an occluded front stalled over the UK, producing precipitation over Chilbolton that lasted almost 12 h. In addition to making polarimetric radar measurements of the deep ice cloud on this day with CAMRa, the Facility for Airborne Atmospheric Measurements (FAAM) BAe-146 aircraft also made in situ measurements. Furthermore, Doppler spectra were also measured from the vertically pointing Copernicus 35 GHz Doppler radar, also situated at the Chilbolton Observatory.

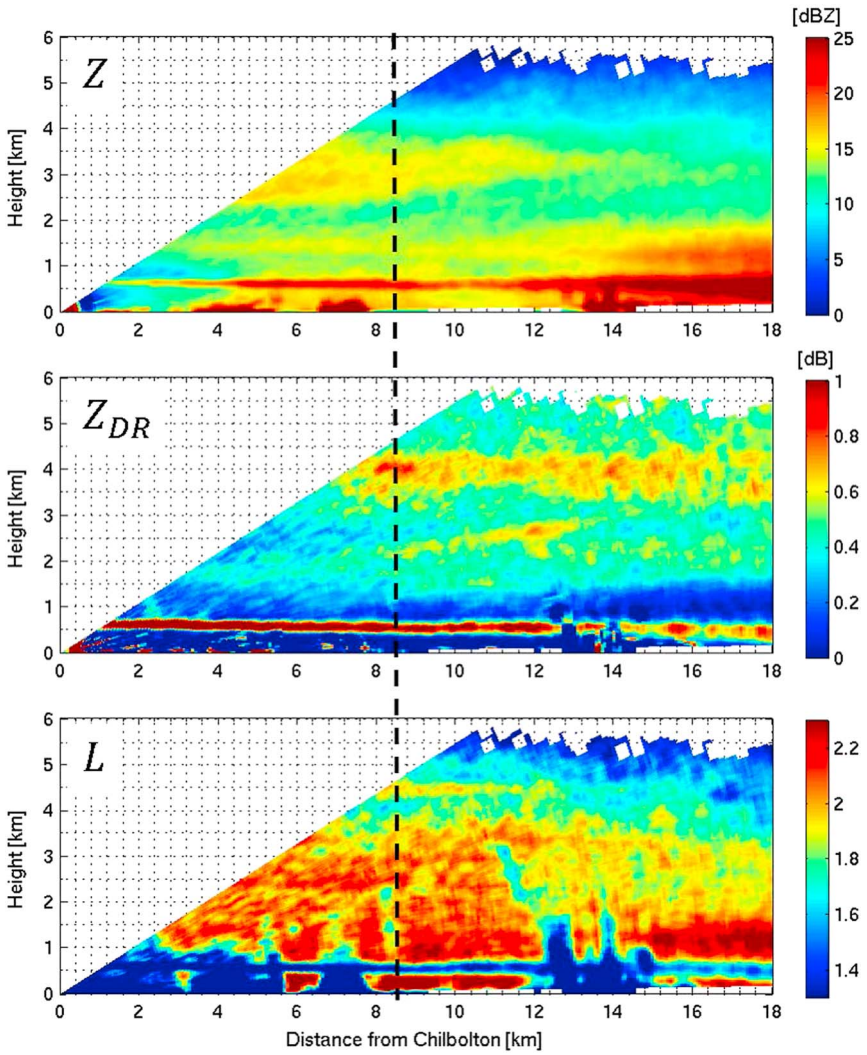

Figure 10. RHI scans of Z, Z_{DR}, and L at 1156 UTC on 17 February 2016. Data have been averaged to 1° and 300 m in range and is only shown for SNR > 10 dB. Areas of low L (up to a height of 2 km between 12 and 15 km in range) is the result of ground clutter; the signature of interest is located at ≈ 4 km.

Figure 10 shows the observed Z, Z_{DR}, and L for an example RHI scan taken at 1156 UTC. The melting layer can again be clearly identified by the enhanced Z, Z_{DR}, and decreased L at approximately 500 m in height. As in case study I, a polarimetric signature of enhanced Z_{DR} and decreased L is seen at approximately 4 km in height. However, the increase in Z and Z_{DR} and reduction in L are weaker in this case study. Figure 11 shows the observed profiles of Z, Z_{DR}, and observed and "effective" L at a range of 8.5 km from Chilbolton (black dashed line in Figure 10). We can see that Z_{DR} reaches only ≈ 0.8 dB, and minimum L is ≈ 1.7. L is lower toward the cloud top than in case study I, as the SNR is lower. Evidence of further pristine ice crystal formation and growth is indicated by enhanced Z_{DR} between 2 and 3 km and an increase in Z. Unfortunately, this signal is too weak for a reliable retrieval. It is interesting to note that there also appears to be evidence of ice production at this height from vertically pointing radar Doppler spectra (this is discussed in more detail in section 7.2). A similar feature is also present in the 31 January 2014 case study.

The interpretation of these profiles is broadly similar to that of case study I. At 4.6 km, the temperature is ≈ −15°C; Z is ≈ 7 dBZ, Z_{DR} is ≈ 0.4 dB and L is ≈ 1.9, all of which are consistent with a monodispersed population of small, irregular polycrystals or aggregates. Below, L decreases to ≈ 1.7 at 4.1 km, while Z_{DR} increases to a peak of 0.8 dB at 4 km. Like case study I, the minimum in L appears to be slightly higher in altitude than the peak in Z_{DR}. Below 4 km, Z_{DR} decreases while L increases, indicative of aggregation. Sharp gradients in Z_{DR} and L at 3.2 km (−7°C) and a corresponding increase in Z also suggest rapid aggregation of the pristine crystals.

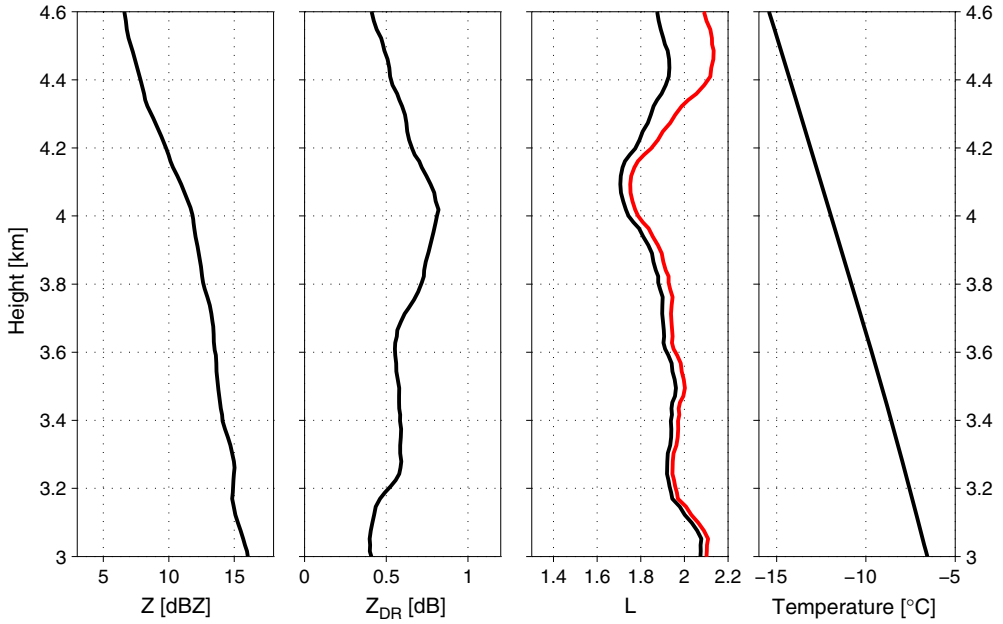

Figure 11. Vertical profiles of Z, Z_{DR}, L, and temperature at 8.5 km in range at 1156 UTC on 17 February 2016 (indicated by dashed black line in Figure 10). The red line is L adjusted for *SNR* effects.

7.1. Retrieval Profiles

As before, C and Z^P_{DRI} are retrieved using look-up tables based on equations (16) and (17) (including a Z^A_{DRI} of 0.15 dB and assuming a fixed pristine oriented crystal aspect ratio). The retrieval profiles are shown in Figure 12. At a height of 4.4 km, C is ≈ −5 dB. After decreasing slightly, it gradually increases until a maximum of −4 dB is reached at a height of 3.9 km. Meanwhile, Z^P_{DRI} gradually increases from 2 dB to its maximum of ≈ 4 dB at 4.1 km, approximately 200 m higher than the peak in C. From there, Z^P_{DRI} decreases to ≈ 3 dB at the location of maximum C (3.9 km), where it remains down to 3.2 km. Microphysically, these profiles can again be explained by plate-like crystals nucleating at ≈ −14°C and growing by vapor deposition, eventually aggregating below. As in case study I, the peak in Z^P_{DRI} is not colocated with peaks in C but, rather, seems to occur above them. For plate-like crystals growing by vapor deposition, it might be expected that they should be colocated, as crystals with larger aspect ratios will both contribute more to Z_h and increase their Z_{DRI}.

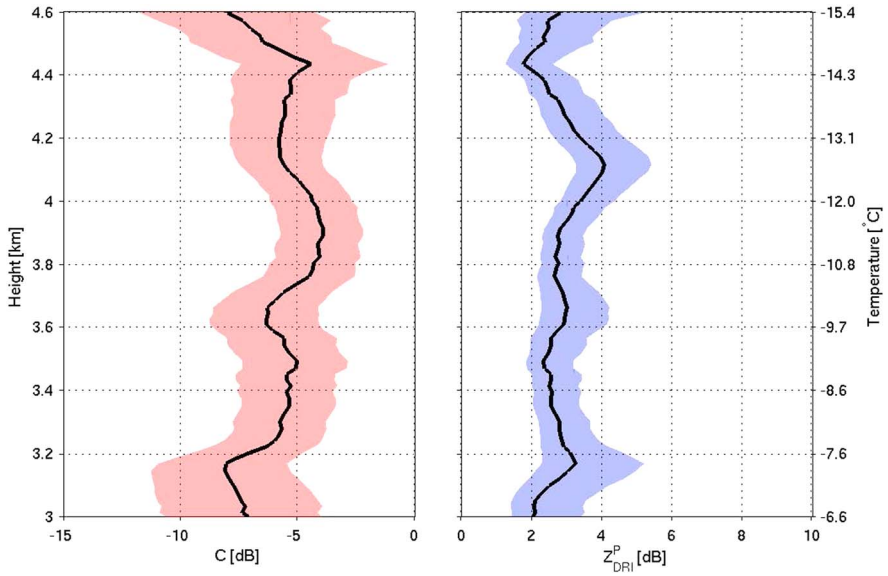

Figure 12. Vertical profiles of retrieved C and Z^P_{DRI} as a function of height and temperature 8.5 km from Chilbolton at 1156 UTC on 17 February 2016. Z_{DR} is assumed to be 0.15 dB.

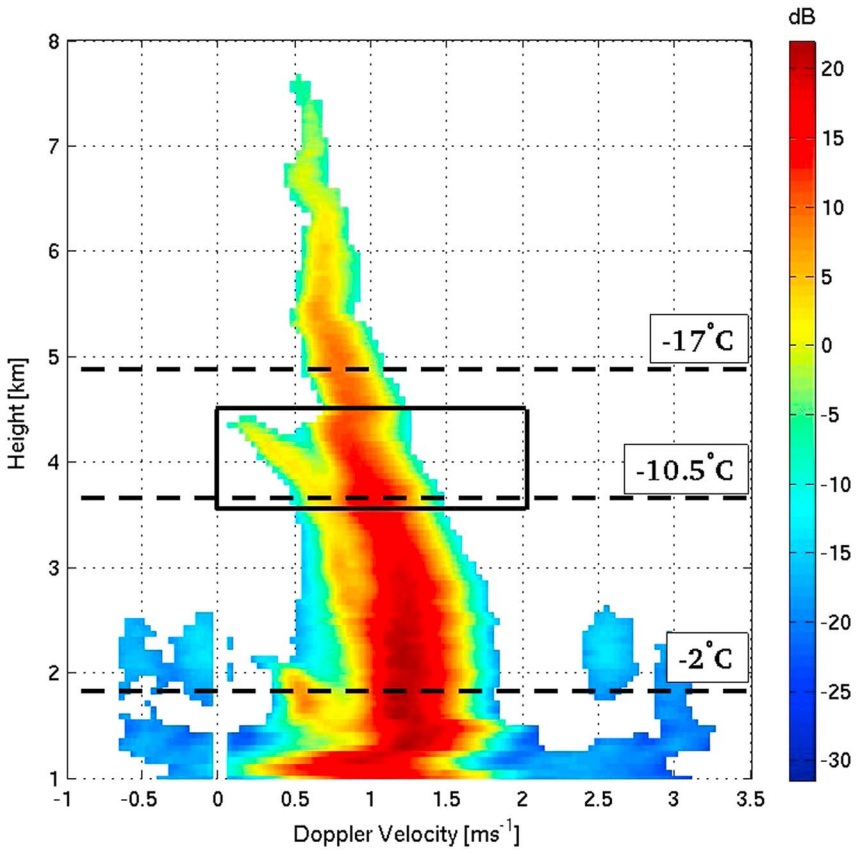

Figure 13. Doppler spectra from the 35 GHz radar at 1238 UTC on 17 February 2016. The box indicates the primary signature of interest. The dashed lines correspond to the flight altitudes of the FAAM BAe-146 aircraft.

However, Z^P_{DRI} is also dependent on the effective particle density. We speculate that the peaking of Z^P_{DRI} above the location of peak *C* occurs because the plates growing rapidly by vapor deposition are initially of high density. The subsequent decrease in Z^P_{DRI} during elevated *C* is indicative of lower density pristine crystals, such as plates with extensions or dendrites. Aircraft imagery shown in section 7.3 support this interpretation.

7.2. Coincident Doppler Spectra

In addition to the polarimetric information collected from CAMRa, the 35 GHz Copernicus Doppler radar also situated at the Chilbolton Observatory was operating at zenith during this case study, measuring full Doppler spectra. Figure 13 shows an example spectograph from 1238 UTC, 42 min prior to the RHI scan in Figure 10. This particular spectrograph is shown as the bimodal feature (which persisted for several hours) is particularly clear. Power is integrated over 10 s for height bins of 30 m. At 7.5 km in height, a single, narrow peak in backscattered power is measured, corresponding to Doppler velocities between 0.5 and 0.6 m s^{-1}. This indicates that hydrometeors producing this backscatter are relatively small and are all falling at approximately the same speed. At ≈ 5.5 km, both the magnitude of the backscattered powers and width of the power spectra increase, indicating that there is an increase in the number and/or size of the ice particles, and a greater spread in their fall speeds. The peak power corresponds to fall speeds of ≈ 1 m s^{-1}. This trend of increasing power and corresponding Doppler velocity continues, which is indicative of these ice crystals growing larger by aggregation. The fluctuation in the power spectra at approximately 1.5 km is likely to be the result of turbulence; observed Doppler velocities also contain contributions from ambient air motions within the cloud. No attempt to correct for these motions has been made.

There are a number of fascinating signatures in this spectrograph. Of primary interest in this paper is the bimodality observed between 3.5 and 4.5 km (indicated by the box in Figure 13), which suggests that at this height there are two distinct ice populations: newly formed pristine crystals (falling slowly) and aggregates or polycrystals (falling more quickly). This feature is observed at the same height as the enhanced polarimetric signatures observed by CAMRa (Figure 10), supporting the interpretation of the retrieval that pristine oriented crystals with large aspect ratios are growing rapidly at these heights by vapor deposition. Their consequent

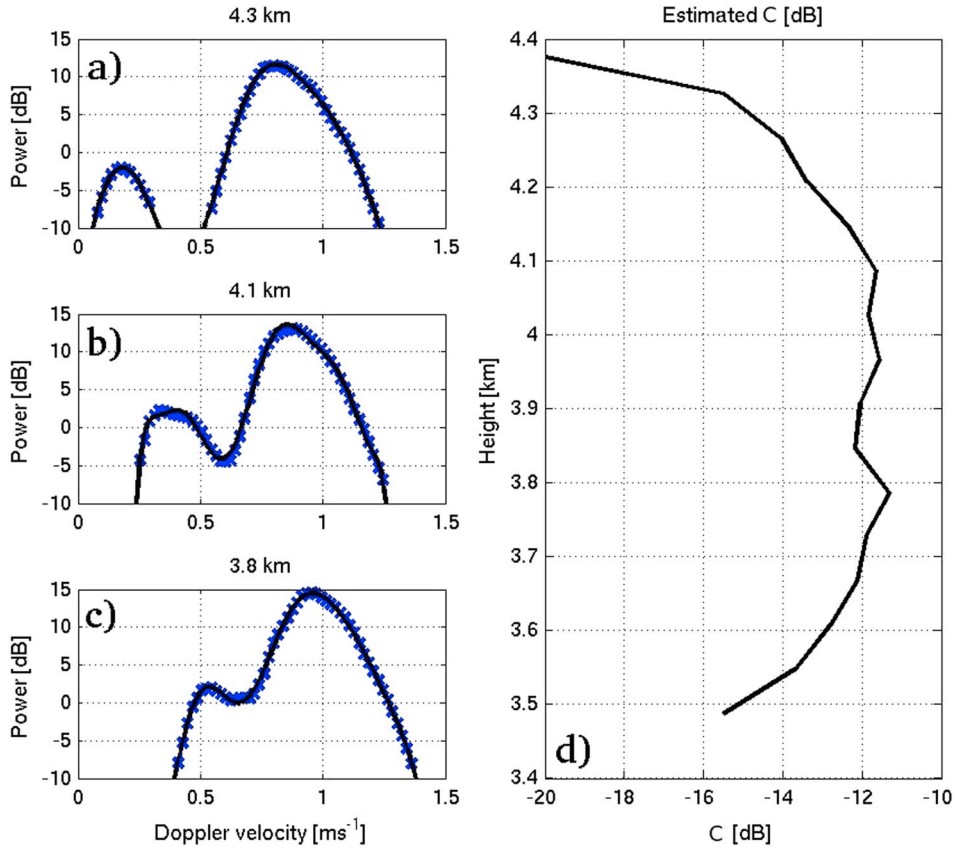

Figure 14. Power distributions at heights of (a) 4.3 km, (b) 4.1 km, and (c) 3.8 km from the Doppler spectra in Figure 13. (d) *C* estimated from these power spectra.

growth (increase in mass) by vapor deposition and later aggregation is illustrated by the gradual increase in the power and the Doppler velocity down to a height of ≈ 3.5 km, where their fall speeds are comparable to the aggregates and the spectrum once again becomes unimodal. However, there is evidence of slight bimodality even down to 2.5 km which would be consistent with elevated Z_{DR} signature observed here by CAMRa. Further, bimodality in the Doppler spectra can be observed between 1.5 and 2.5 km in height.

The bimodality of the spectra between 3.5 and 4.5 km in height provides an opportunity to independently estimate the contribution of the pristine crystals to the radar reflectivity, using a similar method to that used by Rambukkange et al. (2011). The contributions to backscattered power from each ice crystal population were separated using Doppler velocity thresholds. For each crystal type, the radar reflectivity was calculated by integrating the power spectra over velocity ranges of 0–0.4 ms^{-1} at 4.3 km to 0–0.8 m s^{-1} at 3.4 km, the range increasing to ensure that the power backscattered from increasingly faster falling pristine crystals remained separated from the aggregates. Figures 14a–14c show the observed power spectrum (and eleventh-order polynomial fits) at heights of 4.3, 4.1, and 3.8 km, respectively. At 4.3 km, not long after the ice crystals have been nucleated, there is a very clear bimodal power spectrum. By 4.1 km, the pristine oriented crystals have grown larger (indicated by their larger fall speeds), but their peak is still clearly distinguishable from the aggregates. By 3.8 km, the pristine crystals are almost falling at the same rate, leading to an almost unimodal distribution. Figure 14d shows *C* as a function of height estimated using this Doppler spectral method. Qualitatively, *C* estimated with this method behaves very similarly to *C* retrieved using the polarimetric retrieval. The broad maximum in *C* is reproduced at the correct heights, providing evidence that the newly developed polarimetric retrieval technique is capturing the presence and growth pristine oriented crystals at these heights. The magnitude of *C* is lower compared to the polarimetric retrieval; however, direct quantitative comparison is not meaningful for these particular profiles as they are 42 min apart and separated in space by 8.5 km.

7.3. In Situ Aircraft Measurements

Between 1200 and 1400 UTC, the FAAM BAe-146 aircraft, equipped with an array of cloud microphysical probes, made a series of flight runs at temperatures of microphysical interest. The altitudes of these flight runs

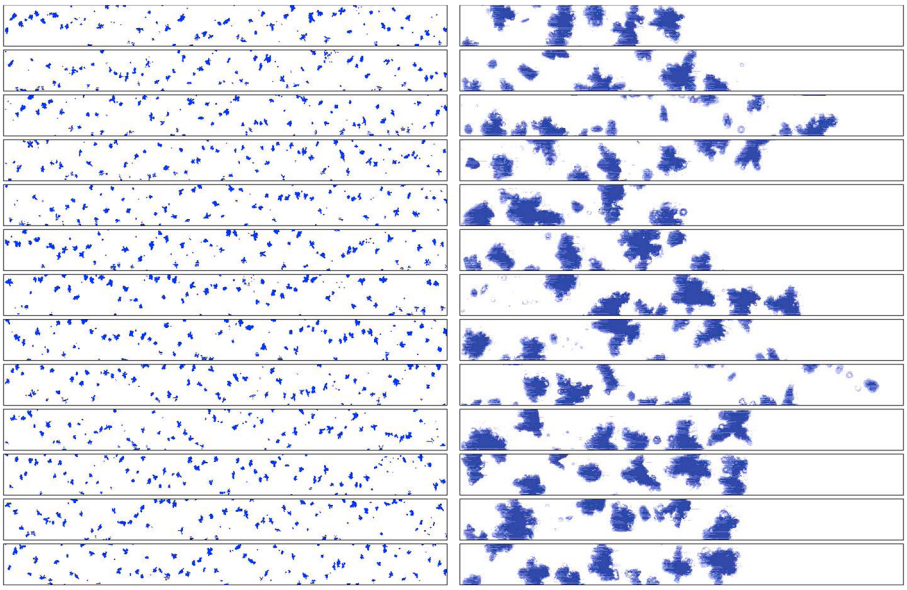

Figure 15. Example (left) CIP-100 and (right) CIP-15 images from the 4900 m (−17.5°C) flight run at 1357 UTC. The image widths are 6400 and 960 μm, respectively.

are indicated by the dashed lines in Figure 13. The quasi-stationary nature of this front means that although these measurements were separated in time, they are assumed to be representative of the microphysics throughout the measurement period. Among the aircraft instruments were 15 μm and 100 μm resolution cloud imaging probes (CIPs): CIP-15 and CIP-100, respectively. These were fitted with antishatter Korolev tips to minimize contamination of the sample area by particle shattering (Korolev et al., 2011). At 1338 UTC, the aircraft made an overpass at 3650 m (−10.5°C) in order to sample the crystals that were producing the bimodal feature. Later, at 1358 UTC, the aircraft made another overpass at 4900 m (−17°C) to sample the crystals that were falling into the region of interest from above.

Figure 15 shows example images from the CIP-100 (left) and CIP-15 cloud imaging probes (right) at 1357 UTC during the 4900 m (−17°C) flight run. The CIP-100 image clearly shows that the ice crystals present at this temperature are small irregular polycrystals and aggregates, with typical major dimensions of 1 mm, with

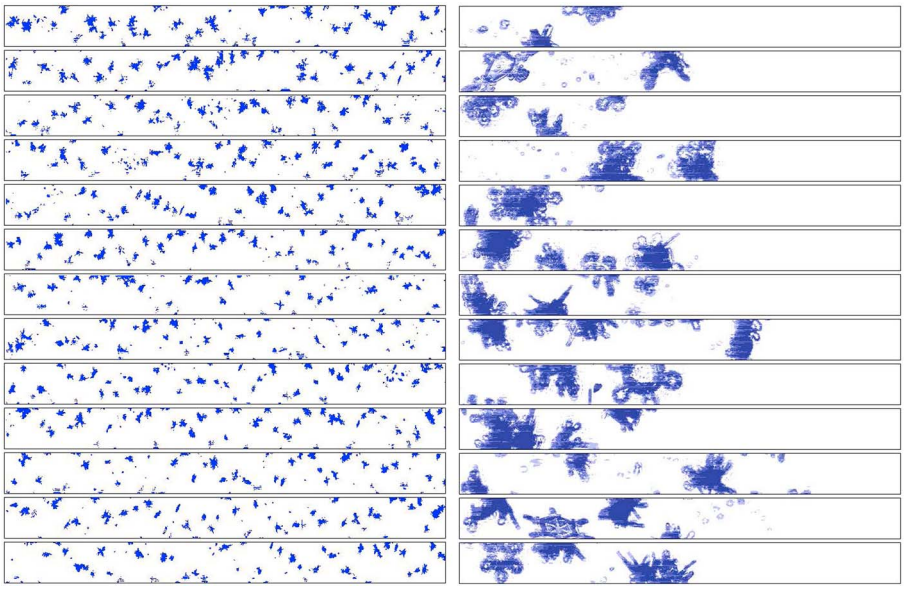

Figure 16. Example (left) CIP-100 and (right) CIP-15 images from the 3650 m (−10.5°C) flight run at 1338 UTC. The image widths are 6400 and 960 μm, respectively.

occasional crystals as large as 2 mm. This is confirmed from the CIP-15 image; the higher resolution of this image reveals the highly irregular nature of these crystals. These crystals likely nucleated at temperatures below −20°C (Bailey & Hallett, 2009) and have fallen to the warmer temperatures in which they are now observed.

Figure 16 shows CIP-100 and CIP-15 images from the 3650 m (−10.5°C) flight level. The CIP-100 image shows that the particles are predominantly irregular and typically larger at this temperature; large polycrystals and some aggregate crystals can be identified. This is consistent with the increase in backscattered power and gradual increase in fall speeds observed in the Doppler spectra. The CIP-15 images reveal that among these crystals, plate-like pristine crystals with extensions (Magono & Lee, 1966) are present. These crystals are likely those nucleated at the height of the bimodal feature (≈ 4.3 km) and have fallen to the height in which they were sampled by the aircraft. The apparent random orientation of these crystals is due to local accelerations as they were drawn into the probe (Gayet et al., 1993). Laboratory experiments show that the branch-like structures observed tend to form when plates crystals grow preferentially at the corners in highly saturated environments, typically between −13.5 and −14.5°C (Takahashi, 2014; Takahashi et al., 1991). This is precisely the temperature in which these crystals have grown. These in situ measurements are further evidence that the conceptual model used in the retrieval is realistic and that the polarimetric retrieval results are physical. It also corroborates the interpretation that reductions in retrieved Z^P_{DRI} while C is elevated are the result of plates growing extensions or branches, which reduces their effective density.

8. Discussion

The bimodal cloud radar Doppler spectra and the in situ aircraft measurements support our interpretation of the polarimetric measurements as regions of formation and growth of new pristine ice crystals and provide encouraging evidence of a physical retrieval. However, the retrieval is sensitive to the choice of aggregate Z^A_{DRI} which we do not know precisely. This is unfortunate, as, in particular for case study II, the polarimetric signatures are relatively weak; all but the strongest are located in the part of the forward model most sensitive to this assumption (Figure 8). In the retrievals, a value of 0.15 dB is chosen, which is the middle of the range of Z_{DR} thought to be typical for aggregates (Ryzhkov et al., 2005; Ryzhkov & Zrnic, 1998a). Ideally, this value should be constrained or measured, for example, by using the observed Z_{DR} above the region of embedded pristine oriented crystal growth. This is difficult in practice as the state of aggregation of pristine crystals is not known a priori, so there is no obvious height at which to sample this "background" Z_{DR}. There is observational evidence that the background Z_{DR} above the embedded mixed-phase regions of interest is, in fact, larger than the Z^A_{DRI} used here. This is supported by observations of $Z_{\mathrm{DR}} > 0.3$ dB in regions that exclusively contain a monodisperse population of irregular polycrystals and aggregates (as seen in the CIP-15 and CIP-100 images measured at 4900 m in case study II). It is interesting to note that an underestimated Z^A_{DRI} would lead to systematically smaller C retrievals from the polarimetric technique, which would bring them into closer agreement with comparable C estimates from the Doppler spectra. However, their imperfect colocation means they may not be expected to necessarily agree. Furthermore, an underestimated Z^A_{DRI} would also lead to an overestimate in retrieved Z^P_{DRI}. It would be interesting to investigate whether this value can be better constrained. For example, it could be that the Z_{DR} of aggregates and polycrystals would be better characterized as a function of temperature.

The relatively large retrieval uncertainties (particularly for case study II) result from, in part, the fact the profiles are derived from RHI scans with an S-band radar. The data have been spatially averaged, but the extent of this averaging is limited so that one can safely assume that the microphysics remains unchanged over the chosen area. The measurement uncertainties on L and Z_{DR} are a function of the number of independent I and Q samples from which they are calculated, defined in equation (4). Thus, the use of a longer dwell time (either through a fixed elevation angle dwell or reduced antenna scan rate), or shorter wavelength would increase this number and reduce retrieval uncertainty; this should be considered for future studies.

It is possible that the "background" aggregates and the newly formed pristine oriented crystals could be subjected to riming as they fall through the SLW layer. The effect of riming would be to reduce the asymmetry of both the aggregates and pristine oriented crystals (Pruppacher & Klett, 1997). The net effect would be to reduce the strength of the polarimetric signal, and therefore C and Z^P_{DRI}. It is evident from the aircraft particle imagery that riming is not occurring in case study II; this is also supported by investigation of the Doppler spectra in Figure 13 which shows particles falling no faster than 1.5 m s^{-1}, which is slower than would be the case if riming were occurring (Locatelli & Hobbs, 1974). The same is true when looking at the mean Doppler velocity profile from the Copernicus cloud radar at the time of the RHI in case study I. However, if uniform riming were occurring, the retrieved C and Z^P_{DRI} quantities would still be valid, as the technique simply separates the con-

tributions to radar reflectivity of asymmetric particles from more symmetric particles, regardless of the reason they have their shape. However, the microphysical interpretation of the retrieved quantities would be different between rimed and unrimed cases.

The retrieval assumes that pristine oriented crystals have a fixed aspect ratio (and by defining ρ_{hv}^{P} in equation (21), it is demonstrated that the retrieval is relatively insensitive to this assumption). Therefore, $\rho_{hv}^{P} = 1$ is assumed in the presented retrievals. However, this assumption would not hold if the technique is used to retrieve Z_{DRI}^{P} in regions that are known to be columns (such as in Hallett-Mossop ice multiplication zones). Unlike plates, the maximum Z_{DR} that can be produced by a distribution of columns is 4 dB, since they fall with random azimuthal orientation and the total backscatter in the *H* polarization must be integrated over all azimuthal angles (see Figure 1). This random azimuthal orientation also has the effect of increasing the shape diversity of the ice crystals from the perspective of the radar; the observed ρ_{hv} for a mixture of columns only with fixed aspect ratios would be lower than for plates only. Therefore, this effect could be conveniently characterized in the retrieval by modifying the ρ_{hv}^{P} value in equation (21). The ρ_{hv}^{P} would be highest for isometric columns, which would look nearly the same to the radar regardless of azimuthal orientation, and lowest for longer, thinner columns or needles, which would increase the shape variety from the perspective of the radar. In effect, ρ_{hv}^{P} would be a function of Z_{DRI}^{P} for a distribution of columns (with fixed aspect ratios). This is something that would be interesting to develop in future work.

Measurements of the linear depolarization ratio (LDR), which describes the relative magnitudes of the cross and copolar radar reflectivities, were also available during both case studies. Depolarization occurs if the major axes of an ice crystal lie at some nonzero angle to the incident radar beam. Thus, a nonzero radar elevation angle or the flutter of asymmetric ice crystals would result in depolarization, and more symmetric aggregates/polycrystals will result in little or no depolarization. This property was utilized by Wolde and Vali (2001), who used a 95 GHz radar on board an aircraft to characterize ice crystal habit with measurements of Z_{DR} and LDR as functions of radar elevation angle. Their ice crystal habit classifications were made through clouds containing single crystal habits; the retrievals presented here are deliberately made in more complex meteorological conditions. We implicitly assume that there is no flutter of the plate-like crystals (i.e., the true ρ_{hv} of plates (ρ_{hv}^{P}) is equal to 1). It is interesting to note that for case study I in regions of pristine oriented crystal growth, LDR does seem to be approximately 1–3 dB higher than 500–1,000 m below where it is typically −27 dB as the signal is dominated by pseudospherical particles. This lends support to the argument that assuming these are plate-like crystals, they are "fluttering" to some degree. Using a similar approach to that used to derive equations (9) and (13),

$$\mathrm{LDR} = 10\log_{10}\left[\frac{\mathrm{Ldr}^{P} \times c + \mathrm{Ldr}^{A}}{c+1}\right] \tag{24}$$

where Ldr^{P} and Ldr^{A} are the "intrinsic" linear depolarization ratios of the pristine and aggregate crystal populations, respectively, as dimensionless linear ratios (not dB). Taking the peak *C* in Figure 7 (−3 dB) and −27 dB for the LDR of the aggregates, it can be inferred that the LDR of the pristine oriented crystals is < -20 dB to produce the observed signature, suggesting that any fluttering is rather small and not likely to lead to significant changes to Z_{DRI}^{P} or ρ_{hv}^{P}.

Effectively, fluttering would translate into a reduction of ρ_{hv}^{P} (less than 1) in equation (21). It may be possible to use LDR to retrieve the degree of fluttering in circumstances when it is significant.

There is also the suggestion that LDR (and Z_{DR}) decreases slightly with increasing elevation angle, but the inhomogeneity of this feature makes it difficult to distinguish this elevation effect. In case study II the polarimetric signal is weaker; no distinguishable LDR feature is associated with the pristine crystal growth layer.

Unfortunately, the enhanced Z_{DR} and decreased *L* signature observed between 1.5 and 2.5 km in height in case study II was too weak for a reliable retrieval. However, evidence that this signature is associated with new pristine crystal growth comes from clear bimodality in the Doppler spectrograph (Figure 13) at this height. The signature occurs within the range of temperatures in which the Hallett-Mossop process is known to operate (Hallett & Mossop, 1974). This hypothesis is supported by the presence of a large number of needles that are observed by the CIP probes at 1800 m (not shown). In addition, the aircraft Cloud Droplet Probe (CDP) detected the presence of both small (<13 μm) and large (>24 μm) liquid water drops here that are thought to be required for the Hallett-Mossop process to operate (Hallett & Mossop, 1974). In the future, the polarimetric retrieval technique presented could be used to locate and study regions of secondary ice production. In principle, the retrieval could be extended to include three ice crystal populations to investigate

Hallett-Mossop zones (such as those presented in Sinclair et al. (2016)); however, this more complex situation would require at least one additional measurement or assumption. One such additional measurement could be K_{DP}.

It is important to note that the vertical profiles used in the retrieval are obtained from RHI scans and, therefore, contain observations from a range of elevation angles. As the radar elevation angle increases, the *V* polarized wave increasingly samples the same plane as the *H* polarized wave. This means that Z_{DR} measurements of all particles at higher elevations will be reduced from the perspective of the radar. Before the retrieved Z^P_{DRI} signatures can be interpreted microphysically, they should be corrected to the "true" Z^P_{DRI}, $Z^P_{DRI}(0)$, that is, that at horizontal incidence. The peak elevation angles included in the retrieval for case studies I and II are 23 and 28°, respectively. The temperatures at which the polarimetric signatures are observed (and evidence from aircraft imagery during the second case study) show that the pristine crystals in these cases are plate like; therefore, $Z^P_{DRI}(0)$ can be readily calculated using the modified Gans equations of Westbrook (2014). For the elevation angles in these case studies, the average $Z^P_{DRI}(0)$ in the retrieval profiles is approximately 2 dB larger than Z^P_{DRI}. Full details of this correction can be found in the appendix of Keat (2016).

9. Conclusions

A novel polarimetric retrieval technique is developed that uses ρ_{hv} and Z_{DR} to separate the radar reflectivity contributions from pristine oriented crystals from the larger crystals they are forming among, overcoming the well-known "masking" effect of aggregates. The technique allows the intrinsic Z_{DR} of pristine crystals and their relative contribution to radar reflectivity to be retrieved. Two case studies are presented, both of which contain retrieval profiles with broadly similar characteristics. They reveal that enhancements of Z_{DR} embedded within deep ice are typically produced by pristine oriented crystals with large Z^P_{DRI} values between 3 and 7 dB (equivalent to 5–9 dB at horizontal incidence), but with varying contributions to the radar reflectivity. Pristine oriented crystals were nucleated at −14 to −15°C embedded among irregular polycrystals and aggregates in deep ice clouds. They grew rapidly by vapor deposition and later aggregated, indicated by their decreasing relative contribution to the radar reflectivity. The technique can be applied even in relatively poor SNR conditions, at the expense of additional uncertainty in the retrieved profiles.

Coincident Doppler spectra from the zenith pointing 35 GHz Copernicus cloud radar and in situ aircraft measurements during the second case study support the conceptual model used to develop the polarimetric retrieval technique and provide evidence of a physical retrieval. At the height of an enhanced polarimetric signature, bimodal Doppler spectra were observed which indicated the presence of two crystal populations: one falling more slowly (more recently formed pristine oriented crystals with extreme aspect ratios) and one falling more quickly (aggregates). By integrating the power spectrum over the expected velocity ranges for each crystal population, an equivalent *C* is estimated that is qualitatively similar to that retrieved using the polarimetric method. In situ measurements from cloud imaging probes on board the FAAM BAe-146 aircraft show that at the location of the enhanced L-Z_{DR} feature, plate-like crystals with extensions were growing among polycrystals and aggregates, supporting the conceptual model used in the retrieval.

Retrieved *C* and Z^P_{DRI} are shown to be sensitive to the assumption of the Z_{DR} of aggregate crystals the pristine oriented crystals are growing among. A better constraint on this value would be useful to improve the retrieval.

More case studies are required to fully evaluate the retrieval. However, we foresee this technique facilitating further improvements in our understanding of the microphysics of embedded mixed-phase clouds. One interesting avenue of future work would be to combine *C* and Z^P_{DRI} with measurements of K_{DP}, which is only sensitive to the number and shape of aligned particles. For example, Z^P_{DRI} and K_{DP} could be used to estimate ice water contents of the pristine crystals using a method similar to Ryzhkov and Zrnic (1998b). There is also the potential for application in an operational environment, where it could aid the identification of hazardous aircraft icing regions.

Acknowledgments
We would like to thank the staff at the Chilbolton Facility of Atmospheric and Radio Research for operation and maintenance of the 3 and 35 GHz radars. Airborne data were obtained using the BAe-146 atmospheric research aircraft, operated by Airtask and Avalon and managed by the Facility for Airborne Atmospheric Measurements (FAAM), which is jointly funded by the Met Office and National Environmental Research Council (NERC). We would also like to acknowledge Stuart Fox from the Met Office for producing the particle images. Thanks also to Andrew Barrett for supplying code to analyze Doppler spectra from case study II and Anthony Illingworth for his helpful and insightful discussions. Finally, the authors would like to thank the anonymous reviewers for their helpful comments, which have greatly improved this manuscript. Radar data supporting the results presented in this paper are freely available from the University of Reading Research Data Archive at https://doi.org/10.17864/1947.119. The first author was funded by a NERC Studentship, grant NE/K012444/1.

References

Andrić, J., Kumjian, M. R., Zrnić, D. S., Straka, J. M., & Melnikov, V. M. (2013). Polarimetric signatures above the melting layer in winter storms: An observational and modeling study. *Journal of Applied Meteorology and Climatology*, *52*(3), 682–700.

Bader, M. J., Clough, S. A., & Cox, G. P. (1987). Aircraft and dual polarization radar observations of hydrometeors in light stratiform precipitation. *Quarterly Journal of the Royal Meteorological Society*, *113*(476), 491–515.

Bailey, M. P., & Hallett, J. (2009). A comprehensive habit diagram for atmospheric ice crystals: Confirmation from the laboratory, AIRS II, and other field studies. *Journal of the Atmospheric Sciences*, *66*(9), 2888–2899.
Balakrishnan, N., & Zrnic, D. (1990). Use of polarization to characterize precipitation and discriminate large hail. *Journal of the Atmospheric Sciences*, *47*(13), 1525–1540.
Batten, L. J. (1973). *Radar observations of the atmosphere*. Chicago: University of Chicago Press.
Bechini, R., Baldini, L., & Chandrasekar, V. (2013). Polarimetric radar observations in the ice region of precipitating clouds at C-band and X-band radar frequencies. *Journal of Applied Meteorology and Climatology*, *52*(5), 1147–1169.
Bodas-Salcedo, A., Webb, M., Brooks, M., Ringer, M., Williams, K., Milton, S., & Wilson, D. (2008). Evaluating cloud systems in the met office global forecast model using simulated cloudsat radar reflectivities. *Journal of Geophysical Research*, *113*, D00A13. https://doi.org/10.1029/2007JD009620
Brandes, E. A., & Ikeda, K. (2004). Freezing-level estimation with polarimetric radar. *Journal of Applied Meteorology*, *43*(11), 1541–1553.
Bringi, V. N., & Chandrasekar, V. (2001). *Polarimetric Doppler weather radar, principles and applications*. Cambridge, UK: Cambridge University Press.
Bringi, V. N., Seliga, T. A., & Cherry, S. M. (1983). Statistical properties of the dual-polarization differential reflectivity (z_{DR}) radar signal. *IEEE Transactions on Geoscience and Remote Sensing*, *GE-21*(2), 215–220. https://doi.org/10.1109/TGRS.1983.350491
Caylor, J., & Illingworth, A. J. (1989). Identification of the bright band and hydrometeors using co-polar dual polarization radar. *Preprints, 24th Conference on Radar Meteorology* pp. 352–357). Florida, USA: American Meteorology Society.
Cho, H., Iribarne, J., & Richards, W. (1981). On the orientation of ice crystals in a cumulonimbus cloud. *Journal of the Atmospheric Sciences*, *38*(5), 1111–1114.
Comstock, J. M., d'Entremont, R., DeSlover, D., Mace, G. G., Matrosov, S. Y., McFarlane, S. A., … Wang, Z. (2007). An intercomparison of microphysical retrieval algorithms for upper-tropospheric ice clouds. *Bulletin of the American Meteorological Society*, *88*(2), 191.
Doviak, R. J., & Zrnic, D. S. (2006). *Doppler Radar and Weather Observations*. Mineola, New York: Dover Publications, Inc.
Gayet, J.-F., Brown, P. R., & Albers, F. (1993). A comparison of in-cloud measurements obtained with six PMS 2D-C probes. *Journal of Atmospheric and Oceanic Technology*, *10*(2), 180–194.
Giangrande, S. E., Krause, J. M., & Ryzhkov, A. V. (2008). Automatic designation of the melting layer with a polarimetric prototype of the WSR-88D radar. *Journal of Applied Meteorology and Climatology*, *47*(5), 1354–1364.
Goddard, J., Eastment, J. D., & Thurai, M. (1994). The Chilbolton advanced meteorological radar: A tool for multidisciplinary atmospheric research. *Electronics and Communication Engineering Journal*, *6*(2), 77–86.
Gregory, D., & Morris, D. (1996). The sensitivity of climate simulations to the specification of mixed phase clouds. *Climate Dynamics*, *12*(9), 641–651.
Hall, M. P., Goddard, J. W., & Cherry, S. M. (1984). Identification of hydrometeors and other targets by dual-polarization radar. *Radio Science*, *19*, 132–140.
Hallett, J., & Mossop, S. C. (1974). Production of secondary ice particles during the riming process. *Nature*, *249*, 26–28.
Harrington, J. Y., Reisin, T., Cotton, W. R., & Kreidenweis, S. M. (1999). Cloud resolving simulations of arctic stratus: Part II. Transition-season clouds. *Atmospheric Research*, *51*(1), 45–75.
Hogan, R. J., Field, P. R., Illingworth, A. J., Cotton, R. J., & Choularton, T. W. (2002). Properties of embedded convection in warm-frontal mixed-phase cloud from aircraft and polarimetric radar. *Quarterly Journal of the Royal Meteorological Society*, *128*(580), 451–476.
Hogan, R., Francis, P., Flentje, H., Illingworth, A., Quante, M., & Pelon, J. (2003). Characteristics of mixed-phase clouds. I: Lidar, radar & aircraft observations from clare'98. *Quarterly Journal of the Royal Meteorological Society*, *129*(592), 2089–2116.
Jiang, H., Cotton, W. R., Pinto, J. O., Curry, J. A., & Weissbluth, M. J. (2000). Cloud resolving simulations of mixed-phase arctic stratus observed during base: Sensitivity to concentration of ice crystals and large-scale heat and moisture advection. *Journal of the Atmospheric Sciences*, *57*(13), 2105–2117.
Keat, W. J. (2016). *Novel Applications of Polarimetric Radar in Mixed-Phase Clouds and Rainfall*. PhD thesis, University of Reading.
Keat, W., Westbrook, C. D., & Illingworth, A. J. (2016). High-precision measurements of the copolar correlation coefficient: Non-Gaussian errors and retrieval of the dispersion parameter μ in rainfall. *Journal of Applied Meteorology and Climatology*, *55*(7), 1615–1632.
Kennedy, P. C., & Rutledge, S. A. (2011). S-band dual-polarization radar observations of winter storms. *Journal of Applied Meteorology and Climatology*, *50*(4), 844–858.
Klein, S. A., McCoy, R. B., Morrison, H., Ackerman, A. S., Avramov, A., Boer, G. d., … Zhang, G. (2009). Intercomparison of model simulations of mixed-phase clouds observed during the arm mixed-phase arctic cloud experiment. I: Single-layer cloud. *Quarterly Journal of the Royal Meteorological Society*, *135*(641), 979–1002.
Korolev, A., Emery, E., Strapp, J., Cober, S., Isaac, G., Wasey, M., & Marcotte, D. (2011). Small ice particles in tropospheric clouds: Fact or artifact? airborne icing instrumentation evaluation experiment. *Bulletin of the American Meteorological Society*, *92*(8), 967–973.
Korolev, A., Isaac, G., & Hallett, J. (2000). Ice particle habits in stratiform clouds. *Quarterly Journal of the Royal Meteorological Society*, *126*(569), 2873–2902.
Locatelli, J. D., & Hobbs, P. V. (1974). Fall speeds and masses of solid precipitation particles. *Journal of Geophysical Research*, *79*(15), 2185–2197.
Magono, C., & Lee, C. W. (1966). Meteorological classification of natural snow crystals. *Journal of the Faculty of Science*, *2*(4), 321–335.
Mitchell, J. F., Senior, C., & WJ, I. (1989). CO_2 and climate: A missing feedback? *Nature*, *341*(6238), 132–134.
Moisseev, D. N., Lautaportti, S., Tyynela, J., & Lim, S. (2015). Dual-polarization radar signatures in snowstorms: Role of snowflake aggregation. *Journal of Geophysical Research: Atmospheres*, *120*, 12,644–12,655. https://doi.org/10.1002/2015JD023884
Morrison, H., de Boer, G., Feingold, G., Harrington, J., Shupe, M. D., & Sulia, K. (2012). Resilience of persistent arctic mixed-phase clouds. *Nature Geoscience*, *5*(1), 11–17.
Morrison, H., McCoy, R. B., Klein, S. A., Xie, S., Luo, Y., Avramov, A., … Zang, G. (2009). Intercomparison of model simulations of mixed-phase clouds observed during the arm mixed-phase arctic cloud experiment. II: Multilayer cloud. *Quarterly Journal of the Royal Meteorological Society*, *135*(641), 1003–1019.
Morrison, H., Shupe, M., & Curry, J. (2003). Modeling clouds observed at SHEBA using a bulk microphysics parameterization implemented into a single-column model. *Journal of Geophysical Research*, *108*, 4255. https://doi.org/10.1029/2002JD002229
Mülmenstädt, J., Sourdeval, O., Delanoë, J., & Quaas, J. (2015). Frequency of occurrence of rain from liquid-, mixed-, and ice-phase clouds derived from A-Train satellite retrievals. *Geophysical Research Letters*, *42*, 6502–6509. https://doi.org/10.1002/2015GL064604
Pruppacher, R. H., & Klett, J. D. (1997). *Microphysics of clouds and precipitation*. Boston, MA: Kluwer Academic Publishers.
Rambukkange, M. P., Verlinde, J., Eloranta, E. W., Flynn, C. J., & Clothiaux, E. E. (2011). Using Doppler spectra to separate hydrometeor populations and analyze ice precipitation in multilayered mixed-phase clouds. *Geoscience and Remote Sensing Letters*, *8*(1), 108–112.

Ryzhkov, A. V., Giangrande, S. E., Melnikov, V. M., & Schuur, T. J. (2005). Calibration issues of dual-polarization radar measurements. *Journal of Atmospheric and Oceanic Technology*, *22*(8), 1138–1155.

Ryzhkov, A. V., & Zrnic, D. S. (1998a). Discrimination between rain and snow with a polarimetric radar. *Journal of Applied Meteorology*, *37*(10), 1228–1240.

Ryzhkov, A. V., & Zrnic, D. S. (1998b). Polarimetric rainfall estimation in the presence of anomalous propagation. *Journal of Atmospheric and Oceanic Technology*, *15*(6), 1320–1330.

Sassen, K. (1980). Remote sensing of planar ice crystal fall attitudes. *Journal Meteorological Society, Japan*, *58*(5), 422–429.

Schrom, R. S., Kumjian, M. R., & Lu, Y. (2015). Polarimetric radar signatures of dendritic growth zones within Colorado winter storms. *Journal of Applied Meteorology and Climatology*, *54*(12), 2365–2388.

Seliga, T., & Bringi, V. (1976). Potential use of radar differential reflectivity measurements at orthogonal polarizations for measuring precipitation. *Journal of Applied Meteorology*, *15*(1), 69–76.

Senior, C., & Mitchell, J. (1993). Carbon dioxide and climate. The impact of cloud parameterization. *Journal of Climate*, *6*(3), 393–418.

Sinclair, V. A., Moissev, D., & von Lerber, A. (2016). How dual-polarization radar observations can be used to verify model representation of secondary ice. *Journal of Geophysical Research*, *121*(18), 10,954–10,970.

Solomon, S., Qin, D., Manning, M., Chen, Z., Marquis, M., Averyt, K., … Miller, H. (2007). *Contribution of working group I to the fourth assessment report of the Intergovernmental Panel on Climate Change, 2007*. Cambridge, UK: Cambridge University Press.

Stoelinga, M. T., Locatelli, J. D., & Woods, C. P. (2007). The occurrence of "Irregular" ice particles in stratiform clouds. *Journal of the Atmospheric Sciences*, *64*(7), 2740–2750.

Sun, Z., & Shine, K. (1994). Studies of the radiative properties of ice and mixed-phase clouds. *Quarterly Journal of the Royal Meteorological Society*, *120*(515), 111–137.

Tabary, P., Le Henaff, A., Vulpiani, G., Parent-du Châtelet, J., & Gourley, J. (2006). Melting layer characterization and identification with a C-band dual-polarization radar: A long-term analysis. *Proceedings 4th European Radar Conference* (pp. 17–20). Barcelona, Spain: ERAD Publication Series.

Takahashi, T. (2014). Influence of liquid water content and temperature on the form and growth of branched planar snow crystals in a cloud. *Journal of the Atmospheric Sciences*, *71*(11), 4127–4142.

Takahashi, T., Endoh, T., Wakahama, G., & Fukuta, N. (1991). Vapor diffusional growth of free-falling snow crystals between −3 and −23°C. *Journal of the Meteorological Society of Japan*, *69*(1), 15–30.

Tang, L., Zhang, J., Langston, C., Krause, J., Howard, K., & Lakshmanan, V. (2014). A physically based precipitation–nonprecipitation radar echo classifier using polarimetric and environmental data in a real-time national system. *Weather and Forecasting*, *29*(5), 1106–1119.

Westbrook, C. (2014). Rayleigh scattering by hexagonal ice crystals and the interpretation of dual-polarisation radar measurements. *Quarterly Journal of the Royal Meteorological Society*, *140*(683), 2090–2096.

Westbrook, C., Ball, R., Field, P., & Heymsfield, A. J. (2004). Theory of growth by differential sedimentation, with application to snowflake formation. *Physical Review E*, *70*(2), 021403.

Westbrook, C. D., & Heymsfield, A. J. (2011). Ice crystals growing from vapor in supercooled clouds between −2.5 and −22°C: Testing current parameterization methods using laboratory data. *Journal of the Atmospheric Sciences*, *68*(10), 2416–2429.

Westbrook, C., Illingworth, A., O'Connor, E., & Hogan, R. (2010). Doppler lidar measurements of oriented planar ice crystals falling from supercooled and glaciated layer clouds. *Quarterly Journal of the Royal Meteorological Society*, *136*(646), 260–276.

Wolde, M., & Vali, G. (2001). Polarimetric signatures from ice crystals observed at 95 GHz in winter clouds. Part II: Frequencies of occurrence. *Journal of the Atmospheric Sciences*, *58*(8), 842–849.